The Astronomical Journal, 168:284 (20pp), 2024 December https://doi.org/10.3847/1538-3881/ad7e18

The Breakthrough Listen Search for Intelligent Life: Galactic Center Search for Scintillated Technosignatures

Bryan Brzycki[1,2], Andrew P. V. Siemion[2,3,4,5], Imke de Pater[1], Carmen Choza[2,3,6], Steve Croft[1,3,6], Vishal Gajjar[1,3], Jamie Drew[6,7], Brian C. Lacki[6], Danny C. Price[6,8], and Sofia Z. Sheikh[2,3,9]
[1] Department of Astronomy, University of California Berkeley, Berkeley, CA 94720, USA; bbrzycki@berkeley.edu
[2] Berkeley SETI Research Center, University of California Berkeley, Berkeley, CA 94720, USA
[3] SETI Institute, Mountain View, CA, USA
[4] Department of Physics and Astronomy, University of Manchester, UK
[5] University of Malta, Institute of Space Sciences and Astronomy, Malta
[6] Breakthrough Listen, University of Oxford, Department of Physics, Denys Wilkinson Building, Keble Road, Oxford, OX1 3RH, UK
[7] The Breakthrough Initiatives, NASA Research Park, Building 18, Moffett Field, CA 94035, USA
[8] SKA Observatory, 26 Dick Perry Avenue, Kensington, WA 6151, Australia
[9] Penn State Extraterrestrial Intelligence Center, 525 Davey Laboratory, The Pennsylvania State University, University Park, PA 16802, USA
Received 2024 August 23; revised 2024 September 20; accepted 2024 September 20; published 2024 November 22

Abstract

The search for extraterrestrial intelligence at radio frequencies has focused on spatial filtering as a primary discriminant from terrestrial interference. Individual search campaigns further choose targets or frequencies based on criteria that theoretically maximize the likelihood of detection, serving as high-level filters for interesting targets. Most filters for technosignatures do not rely on intrinsic signal properties, as the radio-frequency interference (RFI) environment is difficult to characterize. In B. Brzycki et al. (2023), we proposed that the effects of interstellar medium (ISM) scintillation on narrowband technosignatures may be detectable under certain conditions. In this work, we perform a dedicated survey for scintillated technosignatures toward the Galactic center and Galactic plane at the *C* band (3.95–8.0 GHz) using the Robert C. Byrd Green Bank Telescope (GBT) as part of the Breakthrough Listen program. We conduct a Doppler drift search and directional filter to identify potential candidates and analyze results for evidence of scintillation. We characterize the *C*-band RFI environment at the GBT across multiple observing sessions spread over months and detect RFI signals with confounding scintillation-like intensity modulation. We do not find evidence of putative narrowband transmitters with drift rates between $\pm 10\ \mathrm{Hz\ s^{-1}}$ toward the Galactic center, ISM-scintillated or otherwise, above an equivalent isotropic radiated power of 1.9×10^{17} W up to 8.5 kpc.

Unified Astronomy Thesaurus concepts: Technosignatures (2128); Search for extraterrestrial intelligence (2127); Astrobiology (74); Interstellar plasma (851); Interstellar scintillation (855); Astronomy data modeling (1859); Maximum likelihood estimation (1901)

1. Introduction

The Search for Extraterrestrial Intelligence (SETI) is the organized effort to detect technosignatures, signatures that would unequivocally indicate the existence of alien technology. Over the past few decades, SETI has expanded massively in scope, due to technological innovation and an influx of resources. Radio SETI in particular has seen significant advances, using radio telescopes across the Earth, including large antenna arrays, recording wide swaths of instantaneous bandwidth, and digitizing high time and frequency resolutions supported by advancements in data storage and pipelining (P. Horowitz & C. Sagan 1993; P. R. Backus et al. 1997; J. Tarter 2001; P. Backus & Project Phoenix Team 2002; A. P. V. Siemion et al. 2013; G. R. Harp et al. 2016; J. Hickish et al. 2016; J. E. Enriquez et al. 2017; R. H. Gray & K. Mooley 2017; D. C. Price et al. 2020; C. D. Tremblay & S. J. Tingay 2020; V. Gajjar et al. 2021; J.-L. Margot et al. 2021; C. Choza et al. 2023; M. A. Garrett & A. P. V. Siemion 2023; Y. Uno et al. 2023). Radio SETI is complemented by optical SETI, which has sought to detect extrasolar laser emission and anomalies in time-domain data sets (R. P. S. Stone et al. 2005; S. A. Wright et al. 2018b; D. Lipman et al. 2019; A. Acharyya et al. 2023; A. Nilipour et al. 2023; B. Rogers et al. 2024; A. Zuckerman et al. 2024). SETI as a field is constantly evolving and becoming increasingly effective in quantifying the progress and implications of searches for technosignatures (J. Tarter 2001; J. T. Wright et al. 2018a).

The Breakthrough Listen (BL) Initiative is the largest concentrated effort in modern SETI to search for technosignatures (H. Isaacson et al. 2017; S. P. Worden et al. 2017). Beginning in 2015, BL has been instrumental in the development and proliferation of modern SETI efforts, from optical to radio. BL has commissioned time on the Robert C. Byrd Green Bank Telescope (GBT) in West Virginia and the CSIRO Parkes telescope in Australia for radio searches (D. C. Price et al. 2018; D. H. E. macMahon et al. 2018) and time on the Automated Planet Finder in California for optical searches (M. V. Radovan et al. 2014; D. Lipman et al. 2019; A. Zuckerman et al. 2023).

Radio SETI has historically focused on the detection of narrowband high-duty-cycle signals, signals that are generally always "on." This largely stems from the assumption that Hz-order signals are not produced by natural sources (since human radio communications signals are narrower in bandwidth than any known astrophysical radio phenomena), and the practicality that high-duty-cycle signals are always present and

therefore can be isolated in the sky and redetected. Recent searches have expanded to target additional morphologies, such as broadband signals and pulsed signals (V. Gajjar et al. 2021, 2022; A. Suresh et al. 2023).

There are a few fundamental difficulties underlying narrowband technosignature searches. For instance, we do not definitively know the kinds of technosignatures that may exist; even if they are present as narrowband radio signals, we do not know the central frequencies, frequency and time modulation patterns (i.e., for communication or information sharing), or even the arrival times of the emission. To address this, modern radio searches typically use wide instantaneous bandwidths, cover many targets with multiple observations, and use big data analysis techniques to detect signals and sort them by interest.

Another major issue is the presence of radio-frequency interference (RFI), anthropogenic emissions that are regularly picked up in the sidelobes of radio telescopes. Even the GBT, which is located in a federally mandated "Radio Quiet Zone," detects a significant population of RFI, which has a large diversity in morphology (D. C. Price et al. 2020; Y. Maan et al. 2021). RFI can originate from cell phones, television, GPS services (satellite), and virtually any digital device. As such, RFI can be both narrowband and broadband, confounding technosignature searches of all kinds. Most of the algorithmic analysis in modern SETI is concerned with differentiating detected signals between plausible technosignatures and terrestrial RFI. The most common methods are the identification of nonzero Doppler accelerations, since that would imply a nonterrestrial frame of reference, and localization on the sky using location-switching observations.

However, we may also be able to use the information present in the intrinsic power detected in radio signals as a discriminant. J. M. Cordes & T. J. Lazio (1991) described how ionized plasma in the interstellar medium (ISM) could scatter narrowband radio technosignatures in the same way as it scatters pulsar emission, an effect that has been readily observed and analyzed in pulsar observations to probe the properties of intervening ISM plasma. Multipath propagation through the turbulent ISM in the so-called strong scattering regime can result in 100% intensity modulations in narrowband signals. At times, constructive interference brings the overall signal intensity many times higher than the scattering-free intensity, which is beneficial for SETI in that this would bring an otherwise undetectable technosignature above a search's signal-to-noise ratio (S/N) threshold.

B. Brzycki et al. (2023) suggested that ISM scintillations may imprint on the signature of high-duty-cycle narrowband signals within the duration of individual observations, resulting in detectable intensity modulations that follow predicted theoretical distributions and could be differentiated from RFI. A narrowband radio signal whose intensity fluctuations are consistent with ISM scattering would be a very strong candidate for a bona fide technosignature, since the physical nature of the fluctuations would necessarily imply an extrasolar origin. To resolve such fluctuations on the timescale of typical radio observations, we must observe through an appreciable column of free electrons. The best direction for this is therefore toward the Galactic center (GC), for which the column of free electrons in ionized plasma is the greatest (J. M. Cordes & T. J. W. Lazio 2002).

Beyond scattering effects, the GC is particularly intriguing to target for SETI. Just as the plasma density is the highest, the stellar number density and therefore number of available sites for life to originate increases toward the GC. From a game theoretic point of view, a plausible common direction of interest for all ETI in the Galaxy should be toward its center (I. S. Morrison & M. G. Gowanlock 2015; V. Gajjar et al. 2021). ETI civilizations willing and capable of sending strong transmitted radio signals as beacons might set up such transmitters at the GC, or those closer to the GC might transmit toward the Galactic anticenter as viewed from their planet so that other civilizations looking toward the GC would detect them. For analogous reasons, ETI may choose to transmit toward the GC. ETI capable of receiving radio signals might therefore point their radio antennas toward the GC to detect such targeted transmissions or even leakage radiation from normal technological activity.

For observable intensity scintillations, narrowband radio signals must travel through enough plasma to hit the strong scattering regime. However, to actually detect these scintillations from background noise, we simultaneously need the detected signals to have a high integrated S/N. Of course, we can only theorize about the energy budget and technological capabilities of ETI for transmitting sufficiently bright beacons. A common framework for discussing such capabilities is the Kardashev scale, which classifies theoretical civilizations based on their available energy budget (N. S. Kardashev 1964). Kardashev Type I civilizations are able to utilize the energy available on their planet (through solar radiation or other means), while Type II civilizations can directly use the full energy provided by their host star. Representative powers for these classifications are about 10^{16} W for Type I and 10^{26} W for Type II (R. H. Gray 2020). Using BL hardware and observational parameters, V. Gajjar et al. (2021) set limits for technosignatures up to a distance of 8.5 kpc from Earth toward the GC with an equivalent isotropic radiated power (EIRP) above 5×10^{17} W, just an order of magnitude above the definition of a Type I civilization.

We expect strong scintillation to manifest for sources at distances on a kiloparsec scale, so scintillated technosignatures emitted anywhere from us toward the GC need only have the energy budget of a Type I civilization to be detectable with our current technology. In fact, since these limits assume an isotropic emitter, the requisite energy budget is even more favorable for a targeted transmitter. For instance, when it was operational, the Arecibo Planetary Radar's *S*-band transmitter had a directional gain of about 10^7 (A. P. V. Siemion et al. 2013). An antenna with this gain at the GC would only need to be powered by a 5×10^{10} W transmitter to match the EIRP limit set in V. Gajjar et al. (2021). While that is beyond the transmitter power that humanity could engineer for continuous transmission, it is a plausible power given an ETI with more advanced engineering capabilities.

In the present work, we conduct a radio narrowband search at the *C* band of the GC and nearby directions through the Galactic plane (GP) in order to search for ISM-scintillated narrowband signals. We apply an ON–OFF directional filter as used in prior SETI searches. In addition, we perform a scintillation analysis on detected signals toward targets in the survey. We also perform this analysis on control pointings toward the north Galactic pole (NGP), in order to comment on RFI properties at GBT and to determine how similar RFI appears to scintillation at the *C* band. In Section 2, we detail our methodology for estimating likely scintillation timescales

and present the observing strategy. In Section 3, we describe the directional and scintillation analysis performed across our observations. In Section 4, we present signal distributions and show examples of signals that passed the initial directional filter. In Section 5, we discuss the results and implications of our analysis, both for the survey targets and for the NGP observations. Finally, in Section 6, we contextualize this survey with regard to prior SETI efforts and suggest future directions.

2. Observations

2.1. Scintillation Estimation with NE2001

Intuitively, we can maximize the likelihood of detecting scintillated technosignatures by observing along the GP, especially toward the GC. However, scintillation timescales can vary by orders of magnitude depending on distance, frequency, and direction on the sky. It is therefore useful to estimate expected timescales so that we can set appropriate observation parameters, such as observation length, time resolution, and frequency resolution.

We derive scintillation scale estimates based on the NE2001 model (J. M. Cordes & T. J. W. Lazio 2002), following the procedure detailed by B. Brzycki et al. (2023). Namely, for each sky direction (l, b) and distance d, we can use the NE2001 model to first estimate the scintillation timescale Δt_d at 1 GHz and 100 km s^{-1} transverse velocity. We can then scale this estimate for any frequency and transverse velocity (V_T), since $\Delta t_d \propto \nu^{1.2} V_T^{-1}$ for strong scattering. We can create a distribution of plausible timescales by Monte Carlo sampling, in which we randomly sample the distances, frequencies, and transverse velocities from prior distributions.

Signals of interest could occur at any frequency in the band, so for C band, we simply use a uniform prior distribution from 3.95–8.0 GHz. Estimating possible diffraction pattern transverse velocities is very complex and depends on many independent variables, so for simplicity, we also choose a uniform prior from 10–150 km s^{-1}, following B. Brzycki et al. (2023). Along a line of sight, however, locations closer to the GC will generally have a higher concentration of stars, so they should be weighted higher. We can create a normalized probability density function (PDF) for distance along the line of sight by using a model for the stellar number density of the Galaxy.

There are a few ways to model the Galactic distribution of stars that may contain radio transmitters. For example, we can convert from models of the Galaxy's stellar mass density with respect to radius and distance from the midplane by making a simplifying assumption of 1 $M_\odot$ per star (B. Brzycki et al. 2023; Y. Uno et al. 2023). In this work, we follow V. Gajjar et al. (2021) and instead use a more direct model of the Galaxy's stellar number density suggested by B. Carroll & D. Ostlie (2007) of the form:

$$n_*(z, R) = n_0(e^{-z/z_{\rm thin}} + 0.085e^{-z/z_{\rm thick}})e^{-R/h_R}, \quad (1)$$

where z is the height from the midplane, and R is the radius from the GC. M. G. Gowanlock et al. (2011) analyzed a set of Galactic number density models and found that $n_*(z, R)$ gave the closest simultaneous fit to both the total stellar disk mass and the observed stellar density in the local neighborhood, where the normalization factor $n_0 = 5.502$ stars pc^{-3}, the thin-disk scale height $z_{\rm thin} = 350$ pc, the thick-disk scale height $z_{\rm thick} = 1000$ pc, and the radial scale length $h_R = 2.25$ kpc.

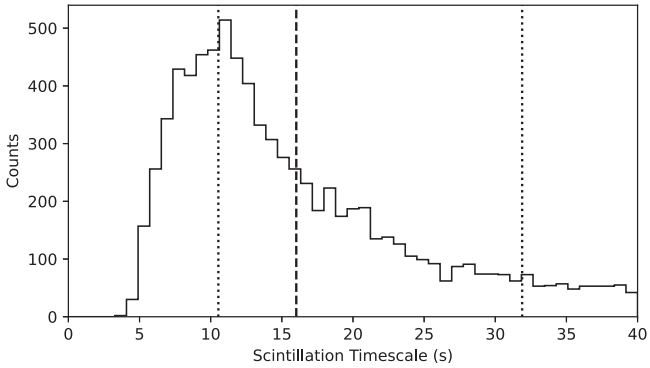

Figure 1. Monte Carlo–sampled scintillation timescales for (l, b) = (1°, 0°) at the C band with $N = 10^4$. The dashed line indicates the median timescale, and the dotted lines indicate the first and third quartiles.

For a line of sight along Galactic coordinates (l, b), we compute weights proportional to the stellar number density starting from a distance $d_{\rm tr}$, the minimum distance for which the strong scattering regime applies to all frequencies in the band, to a specified maximum distance $d_{\rm max}$, in increments of distance Δd. In this work, we take $d_{\rm max} = 20$ kpc and $\Delta d = 0.1$ kpc for the timescale estimates.

One may additionally attempt to model the distribution of ETI transmitter power, either universally or as a function of position in the Galaxy. For instance, for the simplest (and unrealistic) case in which there is a single transmitter power, the inverse square law would heavily skew samples of detectable timescales to those corresponding to smaller distances. On the other hand, a distribution such as a shallow power law would include powers much brighter than average and therefore potentially visible across the Galaxy. For the sampling in this work, we choose not to model the distribution of ETI transmitter power, instead assuming that all possible scintillation timescales are imposed on signals that are detectable (from any direction, distance, and frequency).

For an input direction (l, b), we conduct Monte Carlo sampling with $N = 10^4$ using these independent variable priors to create a theoretical distribution of potential scintillation timescales. These distributions tend to be significantly skewed with long tails, so we use quartiles to characterize the best timescale ranges to target. As an example, Figure 1 presents a histogram of sampled timescales and distribution quartiles for observations toward (1°, 0°) at C-band frequencies.

To help choose target directions for our survey, we repeat this process along a grid near the GC and capture summary statistics for each sky direction's Δt_d distribution. Figure 2 shows each quartile (25%, median, and 75%) of the sampled timescale distribution for $-10° \leqslant l \leqslant 10°$, $-5° \leqslant b \leqslant 5°$, and $\Delta l = \Delta b = 0.°25$. Contours are shown for timescales of 10, 30, 60, and 100 s. In each panel, we notice isolated structures in the sky map, corresponding to the clumps and voids of free electron density present in the NE2001 model, which result in lower and higher timescales, respectively (J. M. Cordes & T. J. W. Lazio 2002).

For any particular sky direction, if our search procedure is designed to detect the range of timescales from the lower quartile to the upper quartile, we are by definition sensitive to 50% of the expected timescales from that direction. While this alone is not particularly comprehensive, it at least provides a point of reference for constraining the long-tailed Δt_d distributions.

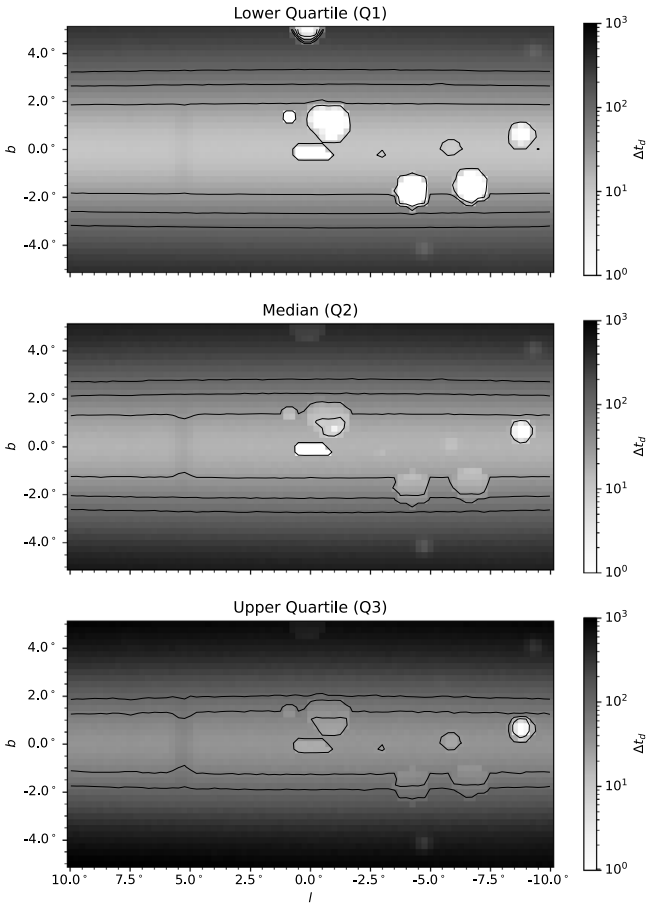

Figure 2. Sky map of the first, second, and third quartiles for scintillation timescale Δt_d, with resolution $\Delta l = \Delta b = 0.^{\circ}25$. Contours are plotted in each panel for timescales of 10, 30, 60, and 100 s. Notice that the 10 s contour in Q1 and the 100 s contour in Q3 bound the majority of the region within 2° of the GP.

2.2. Observing Strategy

We design the survey first by deciding which timescales might be best detected with the BL pipeline at the GBT. However, deciding the range of timescales to which our search should be sensitive is somewhat arbitrary, since it can span many orders of magnitude and there are no clear physical cutoffs. Absent of any practical constraints, sensitivity to scintillated intensity fluctuations intuitively increases with higher time resolution Δt and longer observation times τ. While this would broaden the range of detectable timescales, this comes with a price in terms of data storage and telescope time. This cost is magnified for a survey, where there are many targets, none of which are known a priori to be more likely to harbor technosignatures. The survey must balance covering a wide enough region around the GC while taking detailed observations for each individual target.

While the GC itself is interesting for SETI, the scattering properties toward the GC are still uncertain and potentially at odds with NE2001 predictions (J. M. Yao et al. 2017; A. Suresh et al. 2021). So, we would also like to survey the broader GP, thereby probing other scattering screens. However, the GBT beam size is about 2.′2 at the center of the *C* band (1.′6–3.′2 across the band). Given the small GBT beam size compared to the scale of the GP, a feasible survey with respect to observing time would have to be carried out across a coarser, more widely spaced grid than a survey of the GC only.

Based on Figure 2 and its underlying Monte Carlo simulations, we choose to target timescales from 10–100 s. In Figure 3, we calculate the fraction of sampled timescales in each sky direction covered by this interval, along with contours for 25%, 50%, and 75% coverage. For about $-2^{\circ} \leqslant b \leqslant 2^{\circ}$, over half of the sampled timescales are within this range. In fact, the coverage peaks near $\pm 1^{\circ}$ and dips toward the GP. This is expected; directions along the GP should have shorter scintillation timescales and dip below the lower edge of the interval.

To capture $10\,\mathrm{s} \leqslant \Delta t_d \leqslant 100\,\mathrm{s}$, we base our observation parameters heuristically on these limits. To resolve individual scintles, the time resolution must be a factor smaller than the minimum timescale. Here, we choose a factor of 4, so that $\Delta t \lesssim \Delta t_{d,\mathrm{min}}/4$. Similarly, to capture enough scintles, we choose to require a factor of 5 larger than the maximum timescale, so that $\tau \gtrsim 5\Delta t_{d,\mathrm{max}}$.

Typically, individual BL observations are 5 minutes long, and for narrowband searches, the data is reduced into fine spectral resolution spectrograms with time and frequency resolutions of 18.25 s and 2.79 Hz, respectively. These data products are about 100 GB in total for each *C*-band observation. For narrowband scintillation observations, we keep the same frequency resolution, but extend the observations to $\tau = 10$ minutes and reduce the data to a finer $\Delta t = 2.51$ s. This increases the data size per observation by a factor of 14.6, for a total of 1.6 TB per pointing.

For the GC map, we chose to match the 19 GBT pointings used by V. Gajjar et al. (2021) for the *C* band, observing in the same order as to maximize separation between ON and OFF pointings. This strategy naturally gives a standard of comparison for any interesting detections in our observations. The total on-sky observing time for the GC portion of the survey was thus 6 hr 20 minutes, excluding slew time. For the GP map, we took observations spaced by $\Delta l = \Delta b = 1^{\circ}$ on an 11×5 grid with $-5^{\circ} \leqslant l \leqslant 5^{\circ}$ and $-2^{\circ} \leqslant b \leqslant 2^{\circ}$. Excluding the GC observation already taken, this amounted to 54 new pointings, for a total of 18 hr. These targets are outlined in detail in Table 2 (Appendix A) and are shown overlaid in Figure 3.

For all of these targets, we would like to not only conduct a scintillation analysis, but also apply an ON–OFF directional filter to identify robust candidates. So, we grouped each target into pairs and interleaved 10 minute scans as ABAB cadences. This way, every target received a total of 20 minutes of on-sky time, and signals found within the two 10 minute integrations can be compared in terms of their intensity statistics. Note that since there are an odd number of GC pointings, to include the true GC pointing A00, we observed in the order A00–C01–C07–A00–C01–C07; for all other targets, we observed in alternating pairs.

In addition to these targets of interest, we take an additional observation of the NGP, $(l, b) = (0^{\circ}, 90^{\circ})$, at the beginning of every observing session. Figure 4 shows a histogram of Monte Carlo simulations of scintillation timescales toward the NGP. These are significantly longer than our observation times, so we do not expect to detect ISM scintillation toward the NGP under our observation and data parameters. Note that this does not necessarily mean that strong scintillation is not present in this direction on the sky, but rather that our particular study will not be sensitive to the physical timescales in question. These observations provide a useful control for the RFI environment

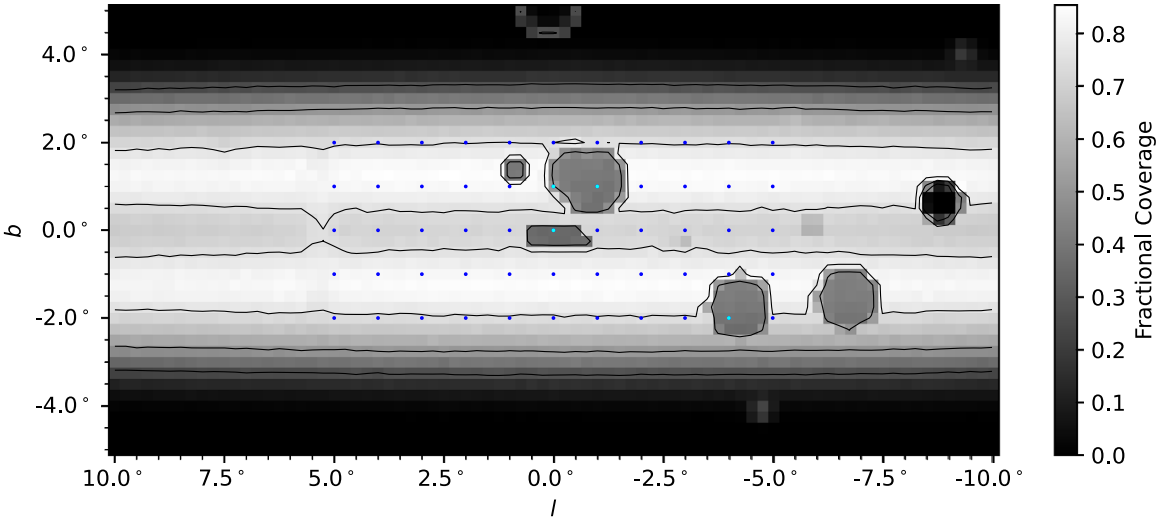

Figure 3. Sky map of the fraction of Monte Carlo–sampled scintillation timescales with $10\,\mathrm{s} \leqslant \Delta t_d \leqslant 100\,\mathrm{s}$, with resolution $\Delta l = \Delta b = 0.^{\circ}25$. Contours for 25%, 50%, and 75% coverage are shown. The blue dots show the GP targets for this survey, where the light blue dots indicate sight lines that pass through regions of enhanced free electron density.

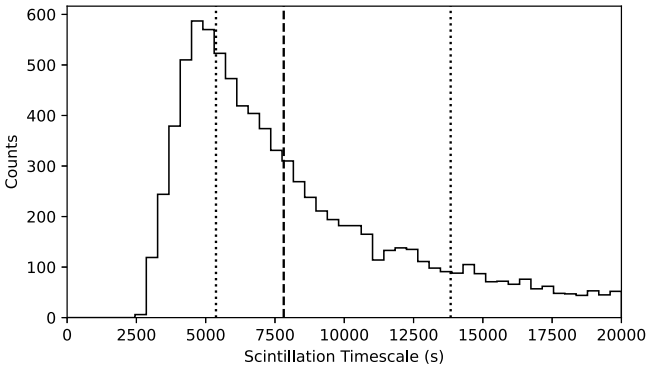

Figure 4. Monte Carlo–sampled scintillation timescales for the north Galactic pole, $(l, b) = (0^{\circ}, 90^{\circ})$, at the C band with $N = 10^4$. The dashed line indicates the median timescale, and the dotted lines indicate the first and third quartiles. As expected, compared to a pointing near the GC (Figure 1), the expected timescales are significantly longer.

for each observing session and further allow for comparison of RFI over time, from session to session.

The GBT observations are processed and digitized as complex voltages by the Breakthrough Listen Digital Recorder, which uses field-programmable gate array boards developed by the Collaboration for Astronomy Signal Processing and Electronics Research (A. Parsons et al. 2006; J. Hickish et al. 2016; D. H. E. MacMahon et al. 2018). These complex voltages are reduced to the final Stokes I intensity spectrogram data products at the target fine resolutions using `rawspec`[10] (M. Lebofsky et al. 2019; B. Brzycki et al. 2022). The survey details, including the start date of the initial NGP observation for each observing session, are summarized in Table 1.

3. Methods

3.1. De-Doppler Search

In Stokes I spectrogram data, narrowband signals with constant intensity appear as thin, continuous features in the time direction. Relative acceleration between the source and receiver causes changes in the Doppler shift of a signal over time, an effect commonly referred to as Doppler drift. Even if the acceleration is cyclic (e.g., part of a planet's orbit or rotation), if the observation time is small compared to the periodicity, the Doppler drift rate will be approximately constant, and the signal path will be linear in time–frequency space (S. Z. Sheikh et al. 2019; M. G. Li et al. 2023).

To find narrowband signals in spectrogram data, we use the de-Doppler code `turboSETI`,[11] which efficiently implements the tree de-Doppler algorithm (J. H. Taylor 1974; A. P. V. Siemion et al. 2013; J. E. Enriquez et al. 2017; E. Enriquez & D. Price 2019). Each signal in the data has an unknown drift rate, so the algorithm integrates spectrograms along a series of trial drift rates in order to find the drift rate that maximizes the detected S/N. We call each detection in an observation a "hit." The essential output from running `turboSETI` are the detected hits' starting central frequencies, drift rates, and S/Ns. We exclude "detections" of the DC bin from each coarse channel, a systematic artifact of the discrete Fourier transform operation used in the voltage reduction process. The output format of `turboSETI` is a plain text table, which can be easily read into Python using the `pandas` package for further analysis (W. McKinney 2010).

Even though the time resolution and observing length are different from previous BL searches, we aim to stay consistent by running `turboSETI` with a purported detection threshold of $\mathrm{S/N} = 10$. However, C. Choza et al. (2023) found that `turboSETI` systematically overestimates its own sensitivity by a factor of about 3.3, so the true detection threshold of this and prior studies is $\mathrm{S/N} = 33$. In fact, brighter detected signals allow for better separation from noise and therefore yield more accurate scintillation statistics, so we elect to continue using these inputs for the detection pipeline in this study.

We run our detection pipeline up to drift rate limits of $\pm 10\,\mathrm{Hz\,s^{-1}}$. The minimum drift rate step used is $\Delta f/\tau \approx 0.004\,\mathrm{Hz\,s^{-1}}$, so about 5000 Doppler drift trials per signal are used for the matched filter. We run `turboSETI` in parallel over spectrogram data distributed across 40 BL compute nodes

[10] https://github.com/UCBerkeleySETI/rawspec

[11] https://github.com/UCBerkeleySETI/turbo_seti

Table 1
Survey Details

Start Target	Start Date (UTC)	Start MJD	No. Targets	Session Target Ranges
NGP0	2023-05-25 03:52:06	60089.16118056	14	GP_L5_B2, …, GP_L3_B-1
NGP1	2023-06-08 02:53:41	60103.12061343	18	GP_L3_B-2, …, GP_L-1_B0
NGP2	2023-07-20 00:14:19	60145.00994213	16	GP_L-1_B-1, …, GP_L-4_B1
NGP3	2023-11-27 15:19:53	60275.63880787	19	GP_L-4_B2, …, GC_C05
NGP4	2024-02-12 10:49:39	60352.45114583	6	GC_C08, …, GC_C12

Note. Session targets follow the initial NGP observation within the same observing session. Observations were taken in ABAB cadences, with targets drawn from Table 2 (Appendix A) in chronological order. The session ranges list the starting and ending targets within a single observing session.

at the GBT, utilizing the GPU on each compute node for additional computational efficiency.

We must note that there are important limitations of this search and signal parameter extraction method. Both because the tree de-Doppler algorithm uses precomputed sums for computational efficiency and because the algorithm is discrete in nature (operating on spectrograms), the algorithm results in errors when the signal drift rate exceeds the unit drift rate $\dot{\nu}_1 = \Delta f/\Delta t$. Since each spectrum is shifted by an integer number of frequency bins based on prior computed shifts, the result is not necessarily a perfect match for a given drift rate, which reduces the received power and therefore recovery efficiency (J.-L. Margot et al. 2021, 2023). According to J.-L. Margot et al. (2021), for our data with $N_t = 600\,\mathrm{s}/2.51\,\mathrm{s} = 239$ time bins, this "dechirping efficiency" drops to 75%, on average. Additionally, for high drift rates ν, with each individual spectrum, signal power will spread across adjacent frequency bins, decimating the dechirping efficiency by a factor of $|\nu/\dot{\nu}_1|$ (B. Brzycki et al. 2022; C. Choza et al. 2023).

3.2. Direction-of-origin Filter

To ensure that signals of interest are localized in the sky, we apply a direction-of-origin (or ON–OFF) filter as a discriminant against local RFI. Narrowband signals that appear as hits in each ON observation and in no OFF observations are considered "events" worthy of manual follow-up inspection.

In this work, we observed our targets in ABAB cadences. So, we perform the ON–OFF analysis on both A and B targets, taking each as the ON direction and filtering for events.

Determining which hits correspond to the same signal can happen in a few ways. To stay consistent with past BL searches, we exclude hits from consideration in which there is a hit in an OFF observation with frequency ν_{off} with

$$\nu_0 - |\dot{\nu}| \cdot 2\tau \leqslant \nu_{\mathrm{off}} \leqslant \nu_0 + |\dot{\nu}| \cdot 2\tau. \tag{2}$$

Similarly, we exclude hits if they do not have a corresponding hit within the appropriate frequency range in the other ON observation.

We note that this type of criteria for ON–OFF filtering has been criticized as unnecessarily broad, since it excludes a relatively large bandwidth that may be occupied by unrelated signals. J.-L. Margot et al. (2021) instead tightened the frequency bounds for related hits and imposed an additional requirement that drift rates must be close across hits to comprise an event (of course requiring that these must not also be satisfied for any hits in OFF pointings). While this approach is significantly more precise for identifying events for ideal linearly drifting narrowband signals, it is not uncommon to observe continuous signals whose component hits vary in drift rate from pointing to pointing. Since these signals often appear in adjacent ON–OFF pairs, they are classified as RFI, but we cannot assume that technosignatures could not exhibit this kind of drift rate variance over similar observational timescales. For instance, transmitters orbiting planets can display continuous drift rate variation even on short timescales, with the magnitude and speed of this variation depending on the orbital period. Whether it is a physical acceleration or an unstable oscillator creating this apparent variation, it may be prudent to relax the assumption that hits belonging to the same signal must have similar fitted drift rates. Narrowband signals in practice can be quite complex, so developing a robust and nuanced approach for identifying technosignature events could be an important avenue for future investigation.

3.3. Scintillation Diagnostic Statistics

To determine whether a signal is ISM scintillated, we must extract and analyze the intensity time series from noisy spectrograms. After a 100% duty cycle signal with constant intensity S is modulated by scintillation, the received total intensity $I_{\mathrm{scint}}(t)$ is given by

$$I_{\mathrm{scint}}(t) = g(t)S + N(t), \tag{3}$$

where $g(t)$ is the scintillation gain and $N(t)$ is the contribution from background noise. Given a signal's starting frequency ν_0 and drift rate $\dot{\nu}$ from the de-Doppler analysis, we follow the procedure described by B. Brzycki et al. (2023) to extract a normalized intensity time series, which ultimately approximates $g(t)$:

1. Select spectrogram frame with a truncated frequency band centered around detected signal. The frequency bandwidth is $N_f\Delta f + \dot{\nu}\tau$, with $N_f = 256$ pixels each of width $\Delta f = 2.79$ Hz.
2. De-drift signal by shifting each spectra in the frame so that the signal is aligned in the frequency direction.
3. If possible, bound the signal by integrating in the time direction and identifying edges of the signal at 1% of the maximum integrated intensity. If the signal bandwidth is too large with respect to the spectrogram size, return to Step 1 with $N_f \leftarrow 2N_f$.
4. Normalize frame over the frequency direction, using the off-signal background.
5. Truncate frame using edges from Step 3 and integrate intensities along frequency direction.
6. Normalize resulting time series to a mean intensity of 1.

We then analyze the normalized time series to determine whether the signal intensities are consistent with strong ISM scintillation. Since scintillation is a stochastic process, taking observations of intensity scintillations can be viewed as

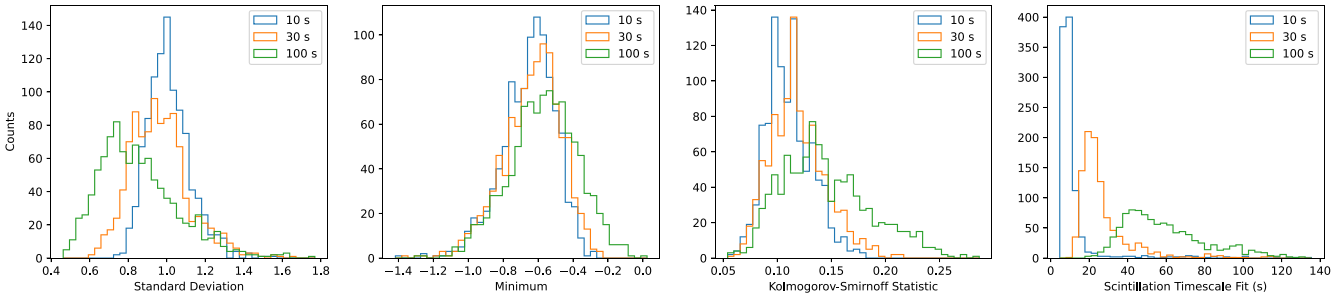

Figure 5. Histograms of diagnostic statistics computed using $N = 1000$ realizations of synthetic scintillated intensity time series embedded in chi-squared radiometer noise. The synthetic observations had $\Delta f = 2.79$ Hz, $\Delta t = 2.51$ s, and $\tau = 600$ s, matching the observations taken in this study. The signals were generated with a bandwidth of eight frequency bins (about 22 Hz) and S/N = 33. Noisy intensity time series were extracted from the synthetic observations and used to compute each diagnostic statistic.

sampling the underlying random process. We must therefore use summary statistics to characterize the specific nature of variability within a signal's intensity time series. We note that since observations are necessarily finite in length, there will always be a certain level of sampling error in these statistics. B. Brzycki et al. (2023) identified a set of "diagnostic statistics" that can help identify the presence of scintillation, including the standard deviation, the minimum, the Kolmogorov–Smirnov (K-S) statistic, and the best-fit timescale to the autocorrelation function (ACF).

The standard deviation, minimum, and K-S statistic probe the expected exponential distribution of intensity gain g due to strong scintillation $f_g(g) = \exp[-g]$, given that the time series is normalized to a mean of 1. Since exponential distributions are well understood, there are expected asymptotic values for each diagnostic statistic in the absence of background noise. Noise can bias these statistics in different ways, but we can use populations of synthetic scintillated signals to empirically determine specific effects as a function of signal parameters, such as S/N and bandwidth.

The best-fit timescale probes the shape of the ACF, which takes the form $\Gamma(\tau) = \exp[-|\tau/\Delta t_d|^{5/3}]$ for lag τ under Kolmogorov turbulence. Once again, due to sampling error, the best fits that we can make with our observations themselves reflect significant variance around the true timescale, Δt_d. As a secondary statistic, this is more difficult to constrain than the statistics used for the intensity distribution, but we can still use synthetic signal populations to investigate this variance (Section 4.1).

These statistics have asymptotic values, i.e., if they were computed over an infinite time series. However, since real observations are finite duration, this introduces natural variance of the estimated statistics around the asymptotic values. For example, in the absence of noise, the standard deviation, minimum, and K-S statistic would have asymptotic values of 1, 0, and 0, respectively; the timescale fit would naturally tend to the true scintillation timescale.

So, it is helpful to simulate scintillated signals embedded in realistic radiometer noise to observe the empirical spread in these statistics as a function of Δt_d. Figure 5 shows histograms of the diagnostic statistics computed over three data sets of synthetic observations corresponding to $\Delta t_d = 10$ s, 30 s, and 100 s, each with $N = 1000$ realizations. The scintillated intensities were generated using `blscint`[12] and injected in synthetic noise with `setigen` at an S/N of 33, matching the sensitivity of the de-Doppler search, with the same time resolution and observation length as our GBT data (B. Brzycki et al. 2022; B. Brzycki 2024).

We notice clear distinctions between marginal distributions as a function of Δt_d, even in the presence of noise. The smaller Δt_d is, the more the intensity distribution appears exponential (clustered near asymptotic values). One peculiarity to notice is that the minimum "intensities" are negative for most realizations. During a trough in a scintillated time series, in which the intensity drops toward 0, subtracting the noise mean from the data in Step 4 will result in negative values if the background noise is below the mean. These negative values are potentially amplified during Step 6, when the time series is normalized to a mean of 1. While this means that this statistic is not quite physical anymore, we can still use it as a feature to characterize the degree to which a signal appears to be scintillated.

4. Results

4.1. Signal Distributions

We conducted a de-Doppler hit search, applied the direction-of-origin filter to find events, and computed scintillation diagnostic statistics over all cadences in our survey. The 54 GP targets comprised 27 cadences, and the 19 GC targets were divided into 10 cadences, in which the triplet A00–C01–C07 was split into two pseudo-ABAB cadences, A00–C01 and C01–C07. Across all observations of the 73 targets (24.3 hr), we detected a total of 1.28M hits and 6018 events. Figure 6 shows examples of detected hits, arranged in ABAB cadences.

We plot the distributions of hit properties such as the detected frequency, drift rate, S/N, and bandwidth in Figure 7. Note that the bandwidths were only estimated as a byproduct of the scintillation analysis, and as such, this is the first time in a narrowband search that we can analyze the bandwidth distribution for large number of detected hits.

We can readily identify a few primary groups of radio emission by frequency; the largest is centered at about 4 GHz, followed by a couple centered at about 4.6 and 8.3 GHz, and perhaps another group at about 7.5 GHz. Note that the histogram counts are plotted on a logarithmic scale. These groups coincide with known regions populated by satellite emissions (C. Choza et al. 2023), so it is very likely that the vast majority of signals found at these frequencies are attributable to RFI.

When we inspect the bandwidth plots in Figure 7, we notice a population of hits over about 6 kHz in detected bandwidth. On inspection, these signals seem to have both narrowband and broadband features; in many cases, the narrowband components are repeated in a comb-like structure. These are detected by the de-Doppler pipeline but do not match the morphology that we

[12] https://github.com/bbrzycki/blscint

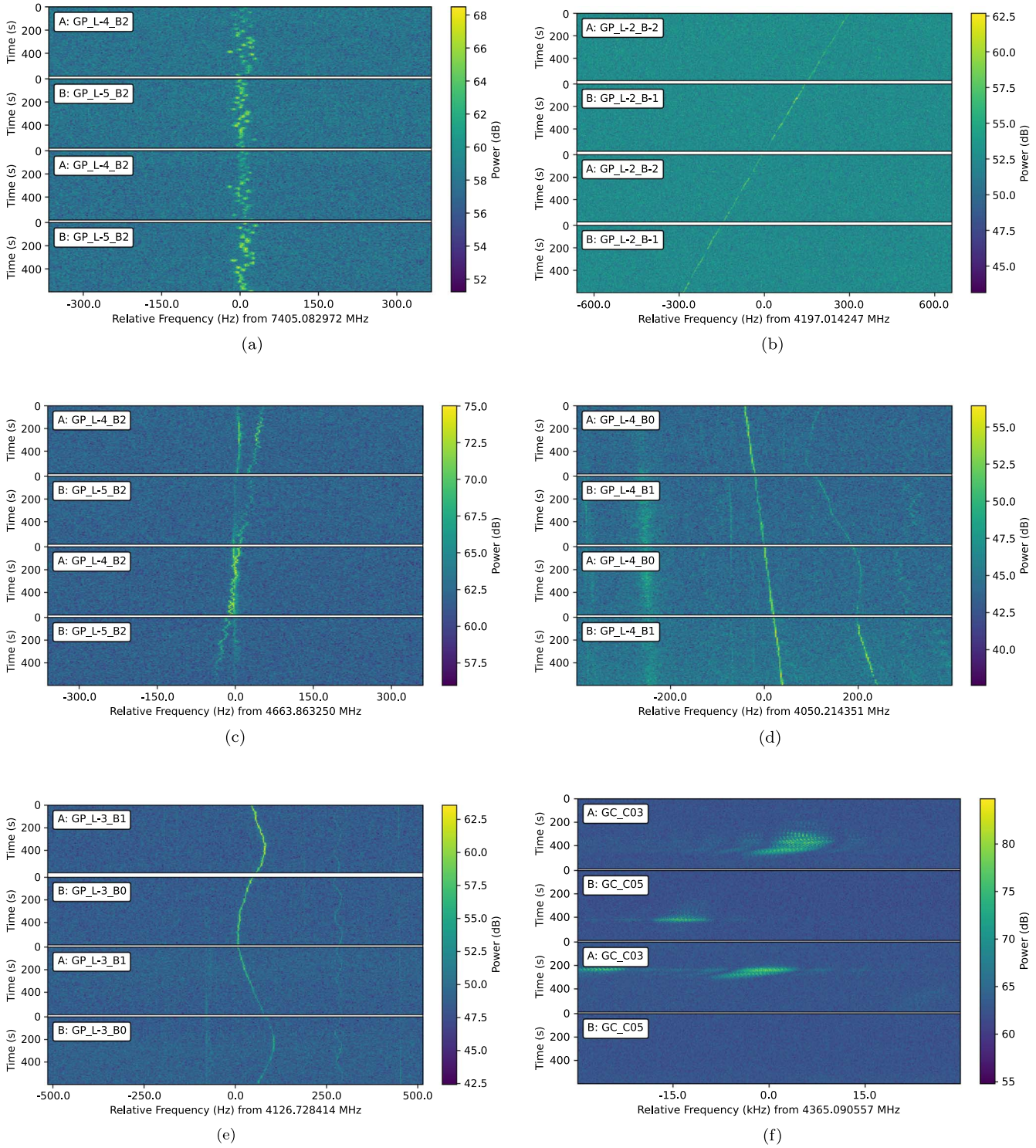

Figure 6. Examples of signals found from the de-Doppler search that passed the algorithmic event filter, but failed manual inspection. Each primary signal appears continuously or with the same morphology in both the ON and OFF scans, indicating that all of the signals are RFI.

expressly search for: high duty cycle narrowband signals. Figure 6(f) is an example with a relatively large measured bandwidth. In these cases, the hit detection reduces to something closer to an energy detection algorithm, and it is still very useful to detect these signals for use in ON–OFF filtering. After all, we do not necessarily know the true morphologies of technosignatures. While previous studies have undoubtedly detected many similar signals in this way, this is the first study to our knowledge that expressly reports on the signal bandwidths as a fundamental step in the analysis.

The peak (mode) of the bandwidth histogram in Figure 7 occurs at about six to seven frequency bins, corresponding to about 20 Hz. So, for our synthetic scintillation distributions in Figure 5, we created the artificial signals with a bandwidth of eight frequency bins as a representative match for a large

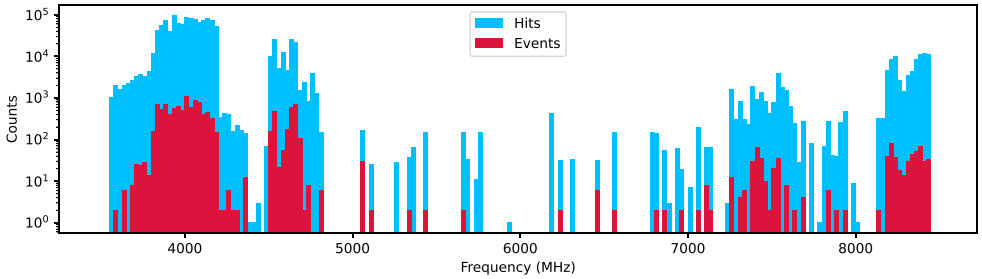

(a) Detected hit and event frequencies

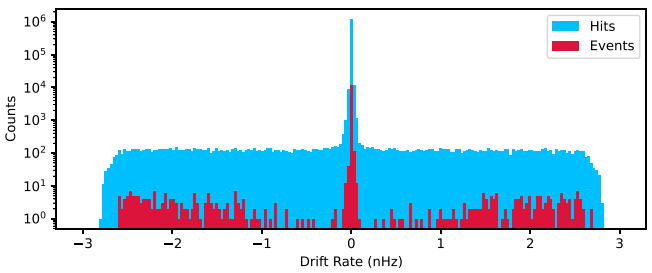

(b) Detected hit and event drift rates

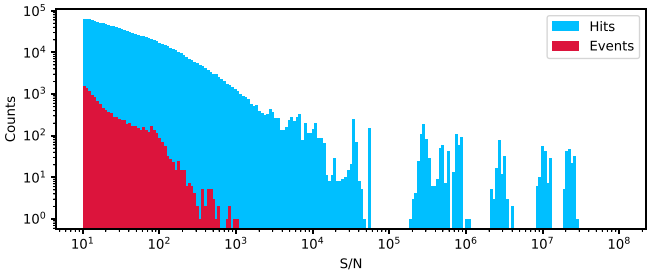

(c) Detected hit and event S/N ratios

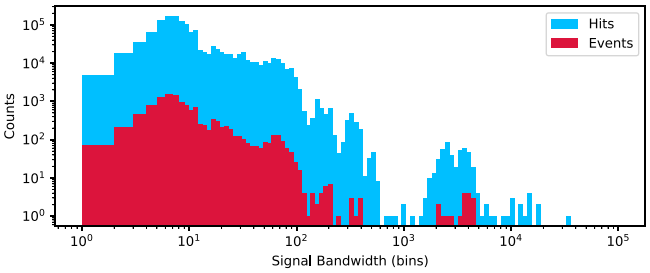

(d) Detected hit and event signal bandwidths

Figure 7. Histograms of frequencies, drift rates, and S/Ns, and bandwidths of all detected hits and events in the GC and GP survey. These plots indicate that the majority of hits and events in our survey (a) are located in frequency regions of known RFI, e.g., 4 GHz, (b) are consistent with terrestrial RFI due to their zero drift rate, (c) approximately follow an inverse power law with respect to detected S/N, and (d) are clustered at a signal bandwidth of seven frequency bins, or about 20 Hz.

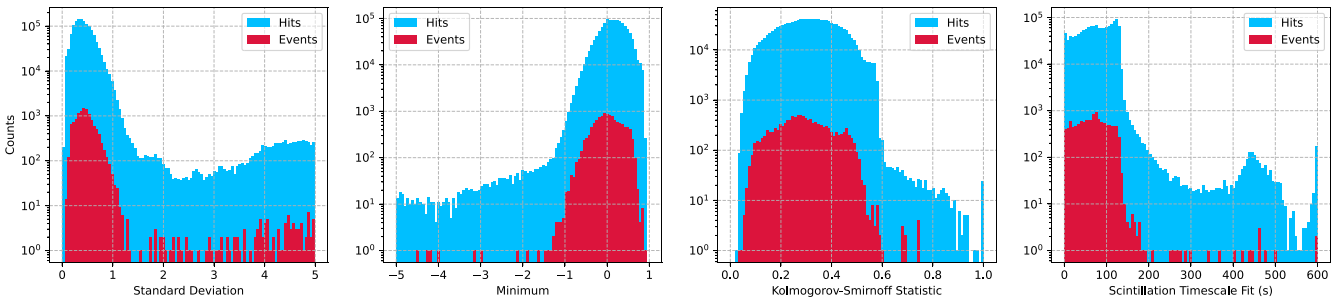

Figure 8. Histogram of diagnostic statistics (standard deviation, minimum, Kolmogorov–Smirnov statistic, and scintillation timescale fit) of detected hits and events throughout all GC and GP observations.

proportion of the detected hits. In the future, it may be useful to match the empirical bandwidth distribution for the creation of synthetic signals, but here we keep the frequency profile consistent across the entire data set.

In Figure 8, we plot histograms of the diagnostic statistics for all detected hits and events. To directly compare these with the synthetic data sets, we normalized these histograms into PDFs by dividing by the bin size and total counts, so that each distribution integrates to 1. We arrive at Figure 9, noting that the density axis is plotted on a linear scale. The event distribution is quite similar to the hit distribution, with only slight excesses toward the parameter space occupied by our theoretical scintillated signals.

4.2. Potential Candidates

We manually inspected all 6018 events that passed our sky localization algorithm. We found that the detected signal is clearly still present in at least one OFF pointing, as is the case

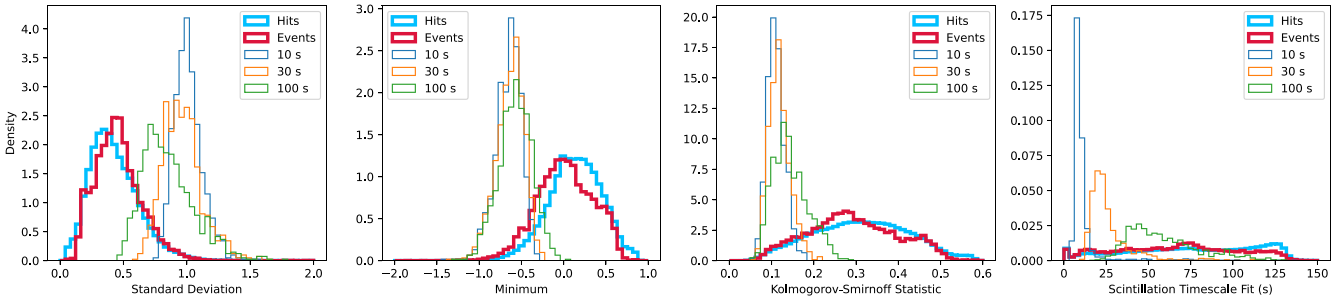

Figure 9. Histogram of diagnostic statistics of detected hits and events throughout all GC and GP observations, compared to the synthetic distributions. Histograms are normalized to integral 1 to directly compare empirical probability densities. There is some overlap between the observed and simulated distributions, with events appearing marginally closer to the simulated distributions, but they are statistically distinct.

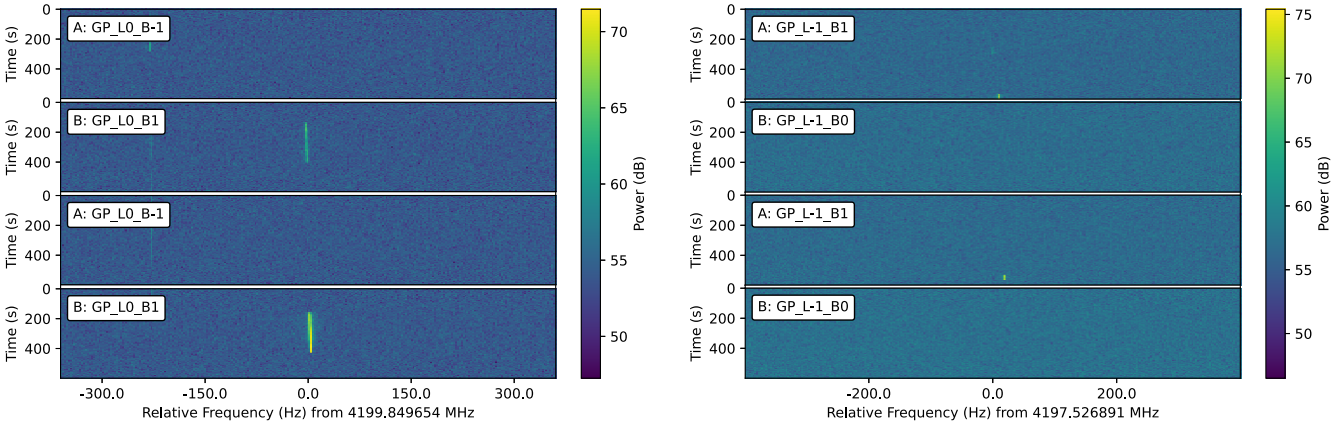

(a) (b)

Figure 10. Best candidates from the direction filter, which passed initial manual inspection.

for each signal in Figure 6, in all but two events. Those candidate events are shown in Figure 10.

It is quite clear that for both events, the detected signal is pulsed, since they do not persist throughout their entire observations. As such, it is possible that these signals are RFI that happened to only emit during the A or B targets of a cadence. While we only took two observations per target, we could check adjacent cadences taken during the same observing session. Since our survey was concentrated relatively close to the GC, if these are RFI signals that were caught in the telescope sidelobes, we would still expect to see them in nearby cadences.

In Figure 19 (Appendix C), we plot four cadences each, all from the same observing session. For event (a), the cadences shown were taken consecutively, and the original detection was the second cadence from top to bottom. It is clear that the pulsed signal is present before and after the cadence of detection, in observations of different targets in the sky, so it must be RFI. Likewise, for event (b), the cadences shown were not taken consecutively, but were all from the same observing session. The original detection is the bottom cadence, but we can see short pulses with the same duration at nearby frequencies in each of the other cadences. Since this signal was also detected in other pointings, we conclude that it is most likely attributable to RFI as well.

4.3. RFI Analysis of NGP Observations

The survey was taken over the course of five observing sessions, so we have five separate 10 minute observations of the NGP (Table 1). As shown in Figure 4, the expected scintillation timescales are quite high compared to our observing length of 600 s; we therefore do not expect to observe real physical scintillations within individual observations toward the NGP, making it a suitable control pointing. However, it is possible that RFI intensity modulations, for communication purposes or otherwise, appear similar to ISM scintillations and therefore confound our directed search. In addition, since we have multiple observations of the same target spaced over months, we can observe any changes in the summary statistics of RFI at each epoch.

Figure 11 stacks the frequency histograms of detected hits in each NGP observation in chronological order. At a glance, we notice the largest changes in frequency occupation in NGP3 versus the other observations, with an excess near 3.6 GHz and a spattering of signals across 4–5 GHz. NGP4 has a noticeable clump of signals near 4.1 GHz. Otherwise, much of the same structure remains over the course of the survey. However, we can also compare these distributions to the frequency distribution of hits detected toward our targets of interest in Figure 7. While there are many more signals plotted for our main survey, there is a noticeable absence of signals between 7.3 and 8 GHz toward the NGP. In Figure 7, the group of signals at 4 GHz has a broader peak and there appears to be a spike of signals near 8.2 GHz that is not present toward the NGP.

We similarly plot histograms of extracted diagnostic statistics in Figure 12. Once again, NGP3 seems the most different, with a spread of signals toward higher standard deviation, lower minima, and high K-S statistics. Here there are significant differences in distributions between the NGP pointings and the survey targets in Figure 8. First, there is a

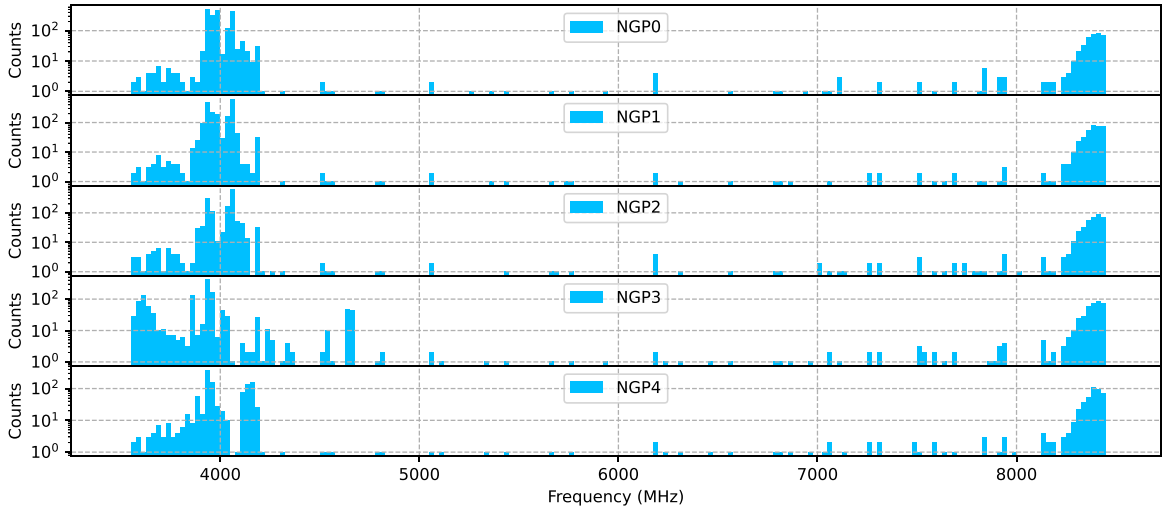

Figure 11. Histogram of frequencies of detected hits in each NGP observation.

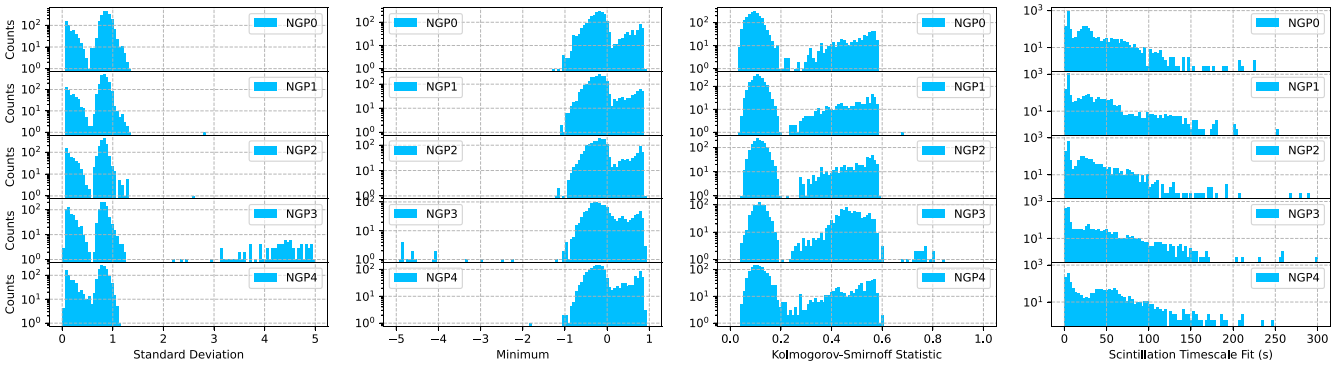

Figure 12. Histogram of diagnostic statistics of detected hits in each NGP observation.

peak in the NGP standard deviations at about 0.9 that is not obvious for the targets. This is a heavily confounding factor, since the ideal asymptotic value for a scintillated signal is 1. Ironically, this confounding peak only appears in a direction for which we do not expect to observe physical scintillations (the NGP) and not in the directions from which we would expect scintillated signals (the GP and GC). Otherwise, the general shapes of statistics distributions are quite different from those for the NGP and are comparatively smoother. Of course, Figure 8 contains the results from 73 different locations on the sky, so this blending is expected.

Overall, NGP3 seems to reflect the most distinct RFI environment for a series of statistics. We note from Table 1 that NGP3 is the most separated from the other observing sessions in time, namely by multiple months in either direction. It is also possible that the time of year is a significant variable for these differences, if RFI at the GBT varies seasonally, but it is difficult to make that claim without additional observations spaced closer in epoch. A longitudinal study on narrowband RFI toward specific regions on the sky, taken with regularly spaced observations, could help explain the nature of variations in RFI as a function of direction and time and help determine whether they are predictable.

4.4. Scintillation Likelihood Weighting

Beyond manually inspecting signals and their statistics, we can use the empirical distributions of diagnostic statistics obtained from synthetic data sets to develop a rudimentary ranking metric for all hits in our search. In other words, we seek to turn the comparisons possible in Figure 9 into a representative weight for each hit.

Since these diagnostic statistics are not likely to be independent, instead of combining each statistic's empirical distribution separately, we seek to estimate the joint PDF over all diagnostic statistics. Note that we can think of each hit, or signal, as a vector of diagnostic statistics, e.g.,

$$\boldsymbol{h} = (h_{\rm std}, h_{\rm min}, h_{KS}, h_{\rm fit}). \tag{4}$$

For each $\Delta t_d \in \{10\,{\rm s}, 30\,{\rm s}, 100\,{\rm s}\}$, we generated a data set with $N = 10^5$ realizations of synthetic scintillated signals embedded in noise, with the same parameters as those represented in Figure 9. We increased N compared to prior synthetic data sets so that resulting models and therefore predictions were more accurate, at the cost of increased computation time. Figure 13 shows corner plots for the scintillation diagnostic statistics over these three data sets, with 2D contours for each pairwise joint distribution. It is apparent that the diagnostic statistics are not independent, especially considering the unique relationship between the K-S statistic and the standard deviation.

For each data set, we used multivariate Gaussian kernel density estimation (KDE) to "fit" a continuous joint PDF $f_{\rm scint}$ as a function of $\boldsymbol{h}$ given Δt_d (D. W. Scott 2015). An alternative to KDE is to compute a multidimensional histogram of the data

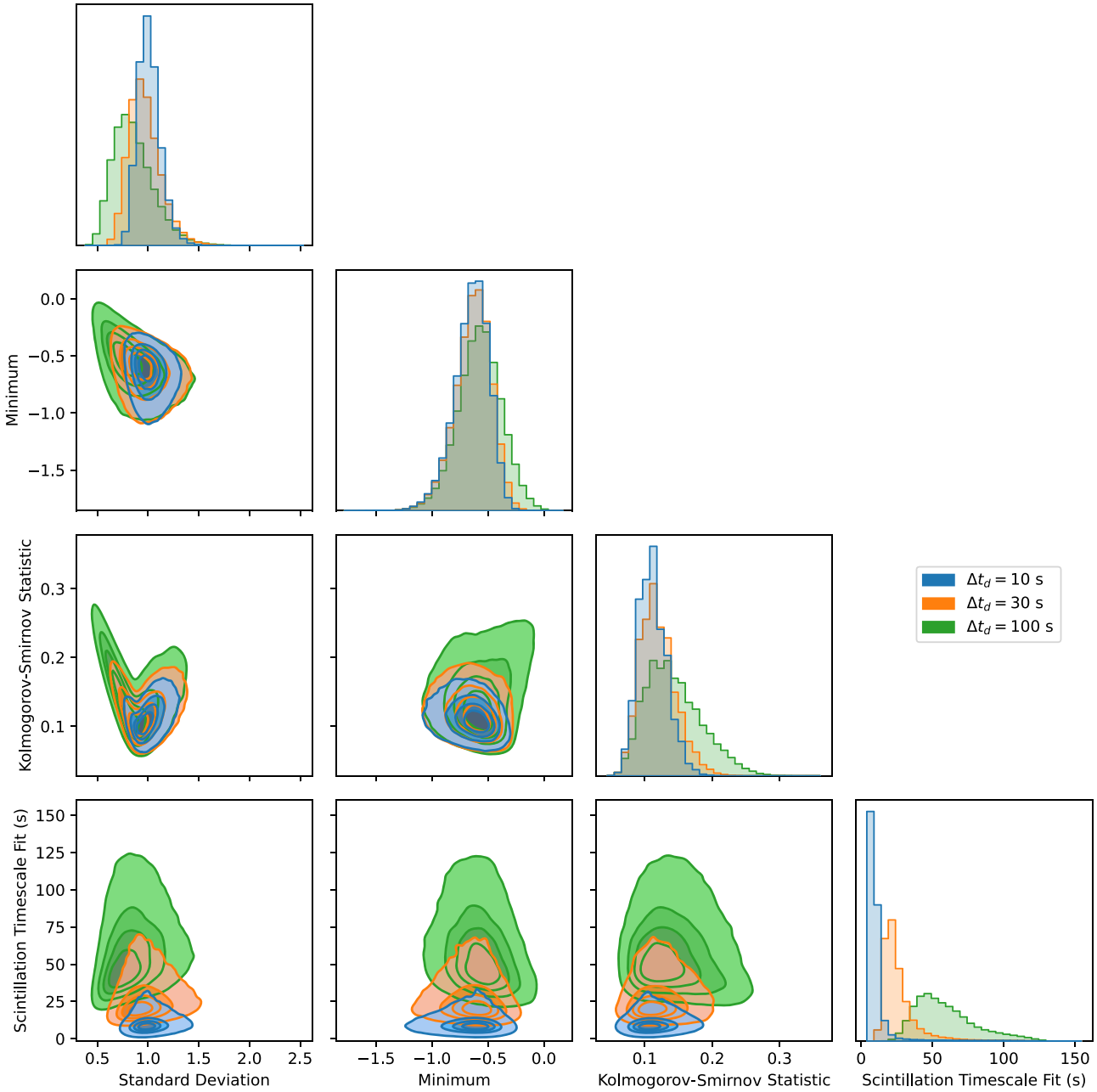

Figure 13. Corner plots comparing distributions of diagnostic statistics for three synthetic injected signal data sets, corresponding to each $\Delta t_d \in \{10\text{ s}, 30\text{ s}, 100\text{ s}\}$. Each data set has $N = 10^5$ samples. Plots on the diagonal show the marginal distributions for each statistic. Off-diagonal plots show 2D contours for the joint distribution of each pair of statistics.

set, where the histogram weights effectively comprise a discrete joint PDF.

The empirical joint PDF f_{scint} can be expressed as a likelihood:

$$\mathcal{L}(\Delta t_d|\boldsymbol{h}) = f_{\text{scint}}(\boldsymbol{h}|\Delta t_d). \tag{5}$$

Then, we can compute a ranking value $w(\boldsymbol{h})$ for any hit with

$$\widehat{\Delta t_d}(\boldsymbol{h}) = \text{argmax}_{\Delta t_d \in \{10\text{ s}, 30\text{ s}, 100\text{ s}\}} \mathcal{L}(\Delta t_d|\boldsymbol{h}) \tag{6}$$

$$w(\boldsymbol{h}) = f_{\text{scint}}(\boldsymbol{h}|\widehat{\Delta t_d}(\boldsymbol{h})). \tag{7}$$

A truly scintillated signal should ideally rank highly when the joint PDF is evaluated for the closest Δt_d. If a hit is clearly not scintillated and its diagnostic statistics are collectively far from the joint PDF, the weight $w(\boldsymbol{h})$ will be very nearly 0. This calculation effectively employs a very coarse maximum likelihood estimation of Δt_d, which is restricted to three values. A future enhancement would be to extend this algorithm toward more values and potentially even toward a continuous range for Δt_d.

We computed $w(\boldsymbol{h})$ over all detected hits that were part of events. Per Equation (6), we estimate the most likely "predicted" timescale $\widehat{\Delta t_d}(\boldsymbol{h})$ for each hit during this analysis, so we can create a confusion matrix comparing the true timescales with these predictions, as in Figure 14. While the majority of signals are classified correctly, there are a nontrivial amount of misclassifications, especially for $\Delta t_d = 30$ s. However, we are only using a discrete set of three true timescales, so

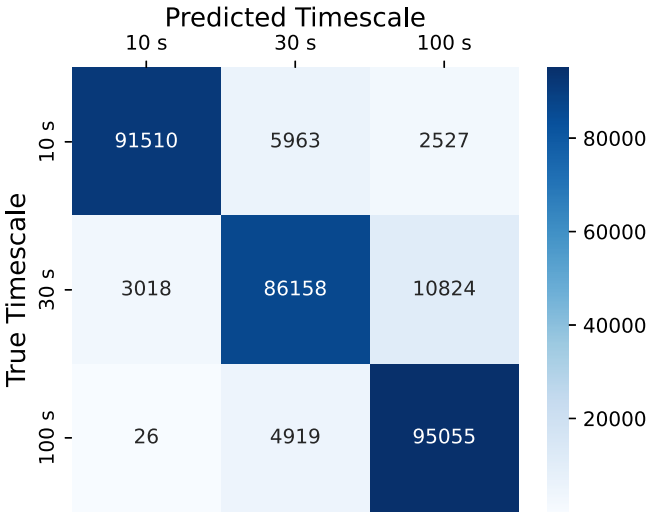

Figure 14. Confusion matrix comparing true scintillation timescales with timescales predicted by the coarse maximum likelihood procedure described in Section 4.4. Each data set is composed of 10^5 synthetic signals.

it makes sense that misclassifications are highest for signal timescales in the middle.

In Figure 15, we plot $w(\boldsymbol{h})$ against frequency for each detected event hit. For reference, we computed rankings for each signal in the synthetic data sets as well and plot those distributions to the right. We readily note the apparent frequency groups of emitters that we identified in Section 4.1. Within each group, hit rankings span multiple orders of magnitude. Unfortunately, they also seem to span the ranking distributions for our synthetic signal data sets. Unsurprisingly, the highest ranked synthetic signals are those with $\Delta t_d = 10$ s.

We present two examples of detected events that contain a highly ranked hit in Figure 16. In these events, the highest ranked hits were the first A pointing for (a) and the first B pointing for (b), with ranking values of 19.7 and 13.8, respectively. Note that these rankings are not probabilities per se, but instead are densities in the joint PDF corresponding to the hits. Visually, these signals appear to exhibit desired scintillation properties, but they appear in both ON and OFF pointings. For both signals, we found $\widehat{\Delta t_d}(\boldsymbol{h}) = 10$ s (Equation (6)).

Though it is relatively simple, the ranking procedure described in this Section allows us to order events for manual inspection based on which are most likely to be scintillated. In fact, while signals with shorter predicted timescales seem to rank more highly in general, we can use this procedure to first group events by closest predicted timescale and then order events within each group for more fine-grained inspection.

5. Discussion

5.1. Search Sensitivity

For Doppler drifting narrowband signals, the minimum detectable flux is given by

$$F_{\rm min} = {\rm S}/{\rm N}_{\rm min}\frac{S_{\rm sys}}{\beta}\sqrt{\frac{\Delta f}{N_{\rm pol}\tau}}, \tag{8}$$

where ${\rm S}/{\rm N}_{\rm min}$ is the detection threshold, $S_{\rm sys}$ is the system equivalent flux density (SEFD), $N_{\rm pol}$ is the number of polarizations, and β is the dechirping efficiency, the factor by which our detected S/N falls off as a result of Doppler drift (V. Gajjar et al. 2021; J.-L. Margot et al. 2023). For drift rates $\dot{\nu}$ that are greater than the unit drift rate $\dot{\nu}_1 = \Delta f/\Delta t$, signal power will smear across adjacent frequency channels within each individual spectrum, resulting in an apparent loss of sensitivity following $\beta \sim |\dot{\nu}_1/\dot{\nu}|$ (B. Brzycki et al. 2022; C. Choza et al. 2023).

To estimate the SEFD for GP targets, we use the measured values provided by the GBT for the C band, where $S_{\rm sys} = 2\,kT_{\rm sys}/A_{\rm eff}$, where k is the Boltzmann constant and $T_{\rm sys}$ is the system temperature (GBT Support Staff 2017). However, GC pointings additionally capture radio continuum emission from the GC background, which must be accounted for in the noise power as $S_{\rm sys} = 2\,k(T_{\rm sys} + T_{\rm GC})/A_{\rm eff}$, where $T_{\rm GC}$ is the brightness temperature corresponding to the GC background. Following V. Gajjar et al. (2021), we use the approximation from K. M. Rajwade et al. (2017) that $T_{\rm GC} \approx (568\ {\rm K})/\nu_{\rm GHz}^{1.13}$.

We can then estimate the minimum detectable EIRP from the inverse square law

$${\rm EIRP}_{\rm min} = 4\pi d^2 F_{\rm min}, \tag{9}$$

for source distance d. For transmitters located at a distance of 8.5 kpc toward GP pointings, we obtain a limit of ${\rm EIRP}_{\rm min} = 1.9 \times 10^{17}$ W. For the maximum drift rates (10 Hz s^{-1}) searched in this study, we will get a larger minimum EIRP by a factor of about $1/\beta \sim 9$, yielding ${\rm EIRP}_{\rm min} = 1.7 \times 10^{18}$ W. For targets at 8.5 kpc toward GC pointings, we obtain ${\rm EIRP}_{\rm min} = 7.5 \times 10^{17}$ W for $\beta = 1$ and ${\rm EIRP}_{\rm min} = 6.7 \times 10^{18}$ W at maximum drift rates, which are higher than those for the GP pointings due to the GC background.

5.2. Figures of Merit

Since there are so many axes of analysis and such a large parameter space intrinsic to SETI, it can be difficult to directly and meaningfully compare technosignature searches. One common way is to use so-called "figures of merit," which assign a representative value toward each study based on their observational search parameters.

The popular Drake figure of merit is given by

$${\rm DFM} = \frac{\Delta\nu_{\rm tot}\,\Omega}{F_{\rm min}^{3/2}}, \tag{10}$$

where $\Delta\nu_{\rm tot}$ is the total observing bandwidth, and Ω is the total sky coverage (F. Drake et al. 1984). By design, the larger this value, the more comprehensive the SETI search. For our study, the DFM is about 1×10^{33} for $\dot{\nu} \leqslant 0.004$ Hz s^{-1}, down to 4×10^{31} for $|\dot{\nu}| = 10$ Hz s^{-1}.

However, the DFM only measures a few aspects of a search and treats each direction on the sky equally, which is especially misleading for our study because the distribution of potential transmitters is likely heavily biased toward the GC. To address these limitations, J. E. Enriquez et al. (2017) developed the continuous waveform transmitter rate figure of merit, defined as

$${\rm CWTFM} = \zeta_{\rm AO}\frac{{\rm EIRP}_{\rm min}}{N_*}\frac{\nu_c}{\Delta\nu_{\rm tot}}, \tag{11}$$

where N_* is the number of observed stars, ν_c is the central frequency, and $\zeta_{\rm AO}$ is a normalization factor such that ${\rm CWTFM} = 1$ when the EIRP matches that of Arecibo's planetary radar. The smaller the CWTFM, the more sensitive

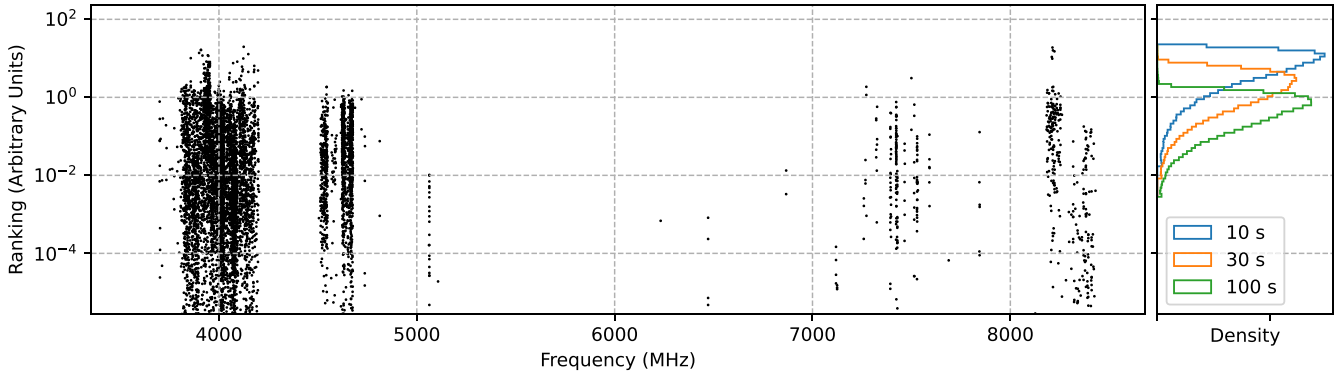

Figure 15. Ranking estimates for all hits in detected events as a function of frequency, with rankings on a logarithmic scale. For comparison, synthetic ranking distributions are shown on the right panel for timescales of 10, 30, and 100 s.

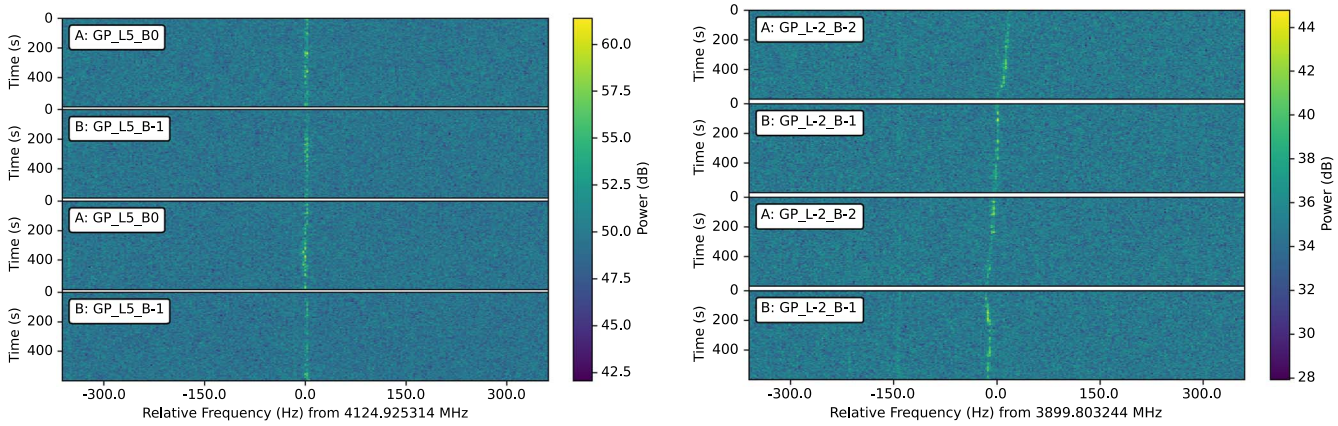

(a) (b)

Figure 16. Examples of signals found from the de-Doppler search that passed the algorithmic event filter and ranked highly on the scintillation analysis.

the study. The portion $\nu_c/(N_*\Delta\nu_{\rm tot})$ is referred to as the "transmitter rate," which encodes information about the portion of frequency space searched and the breadth of targets searched. We estimate the number of stars observed in the survey by numerically integrating Equation (1) along the FWHM of our beams. Up to 8.5 kpc away, we estimate a total of about 6.5 million and 3.5 million stars toward the GP and GC pointings, respectively, yielding CWTFMs of 2.2 and 17.

We plot the transmitter rate against maximum EIRP for this study in Figure 17, along with the results from prior technosignature searches. Since we have a method for estimating the number of stars within our telescope beams and since there is technically no hard distance cutoff, we can actually compute multiple CWTFM ratios as a function of distance through the Galaxy. We start at 0.5 kpc and extend the calculation by steps of 2 kpc until we get to 16.5 kpc, plotting each step as a separate point. We mark the point closest to the GC ($d = 8.5$ kpc) in black for contrast. Also, note that our EIRP limits are computed assuming $\beta = 1$, so for the highest absolute drift rates in the search ($10\,{\rm Hz\,s^{-1}}$), we will get a larger minimum EIRP by a factor of about $1/\beta \sim 9$, indicated by extending the limits to the right at each distance. For the groups of GP and GC pointings (in blue and green, respectively), this effectively builds up a shaded region in the plot, interpolating between EIRP estimates for each distance.

The transmitter rate plot for prior SETI searches evidently shows a rough power-law relationship with the minimum EIRP. This observed pattern is essentially a manifestation of the inverse square law, even though the plotted studies occurred over the span of decades and had different targets and observational configurations. Our 8.5 kpc limit marks the lowest transmitter rate and $\rm EIRP_{min}$ of SETI searches near the Kardashev I scale, pushing the implied power-law limits deeper.

The path of the values plotted depends on the model for stellar number density in our Galaxy; in this case, it seems to have a knee at about 10.5 kpc. Since 8.5 kpc gets the closest to the GC (and contains it), we focus on those EIRP limits as representative for this study, but it is interesting to note the seemingly diminishing returns we get in transmitter rate as we increase in distance and minimum EIRP. Of course, the number density of stars falls off as the distance from the GC increases, but even the search volume expanding with distance does not make up for this.

5.3. Detectability of ISM Scintillation

Comparing ranking values between detected narrowband RFI and synthetic scintillated signals shows us that there is a significant fraction of RFI with scintillation-like modulation statistics (Figure 15). In fact, about 39% of detected event hits have a ranking $w(\boldsymbol{h}) \geqslant 0.0028$, the minimum value for any of the synthetic signals; about 2.3% have $w(\boldsymbol{h}) \geqslant 1$. This implies that our methodology is unable to disentangle certain RFI modulations from true ISM-induced intensity scintillations.

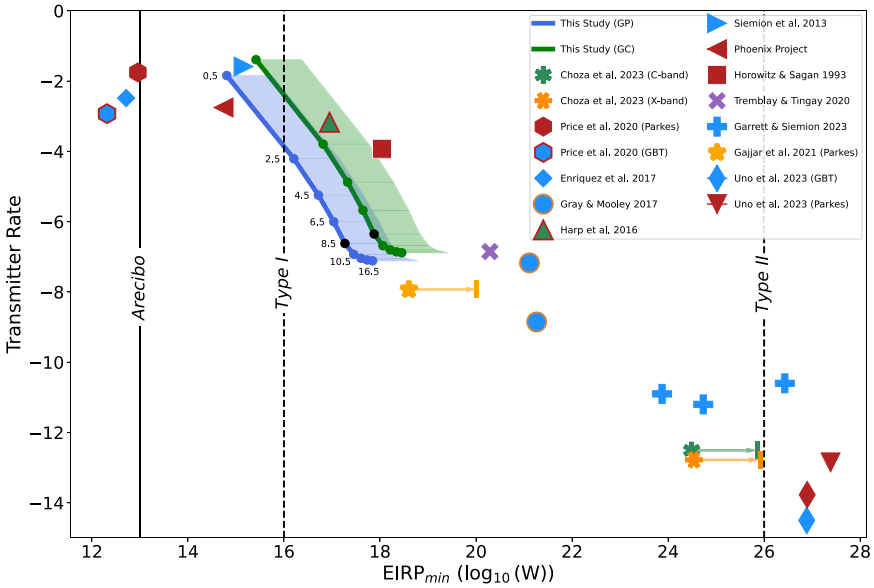

Figure 17. Transmitter rate vs. EIRP for this study and previous radio technosignature searches. EIRP limits for this study at various distances for the GP targets and GC targets are plotted in blue and green, respectively. The EIRP limits for sources up to 8.5 kpc are marked in black. For each distance, we extend EIRP limits up to the right, corresponding to the maximum drift rate of 10 Hz s^{-1} searched in this study, for which $\beta \approx 0.11$. Note that while this study and C. Choza et al. (2023) use S/N = 33 to correct for the offset factor in `turboSETI`, we choose not to alter the results from any earlier studies that may have been affected by this.

This confounding RFI is difficult to characterize precisely, and likely is not homogeneous, but the signals still seem to be concentrated in frequency regions together with non-confounding RFI. Our analysis would undoubtedly benefit from a detailed understanding of the specific forms of RFI modulation present across our observing bandwidth, but this kind of information is not readily accessible or even available beyond the detections that we make within radio astronomy observations. Nevertheless, deducing patterns or classifying signals at the granularity of intensity time series will certainly pave the way for future SETI work that targets scintillation or other detectable forms of intensity (or phase) modulation.

The RFI environment around the GBT is uncertain and dynamic, as we saw in Section 4.3. There seem to be populations of RFI that are more similar to scintillated signals than others, and we seemed to detect a greater proportion toward the NGP. In fact, B. Brzycki et al. (2023) conducted an RFI analysis of the north celestial pole at the *C* band, and found very few signals whose diagnostic statistics coincided with the distributions of synthetic scintillation signals. RFI is generally picked up through the sidelobes of the antenna pattern of radio telescopes, so it makes sense that we will observe some interference (especially from geosynchronous satellites) in certain directions and not in others. Unfortunately, it is difficult to pinpoint the exact origin for any given group of RFI. Since the detected RFI environment seems to systemically vary with observing direction, taking observations of separate sky locations to serve as controls for RFI detection or mitigation may simply be unhelpful or inapplicable. In other words, it may be necessary for RFI occupancy analysis, such as that done by C. Choza et al. (2023), to specifically use data from observations of targets of interest, even though they may contain technosignatures and therefore bias against true positive detections. We must be increasingly careful not to excise technosignature candidates, at the risk of preserving many false positives for manual inspection.

One exciting possibility behind searching for ISM scintillations in narrowband signals was the idea that it would give us a way to classify one-off signals as high-quality technosignature candidates. By convention, SETI searches have required that true candidates both pass the direction-of-origin filter and are detectable on reobservation (S. Z. Sheikh et al. 2021). It is possible that a source transmits for a period of time but drops off: for instance, if an ETI is transmitting toward a set of targets one after another. However, in our analysis, we have detected individual hits in single observations toward the GC and GP that have high scintillation rankings $w(\boldsymbol{h})$. If these were not part of ON–OFF cadences, in which we were able to verify that the signals persisted throughout, we might otherwise consider these signals as potentially modulated by ISM scattering. It seems clear that unless we obtain a detailed understanding of the various intensity modulations present in RFI, we will continue to require sky localization filters. For single-dish telescopes, this requires consecutive, repeated observations, but multibeam observatories can more effectively utilize telescope time by simultaneously observing different pointings for localization (Z.-Z. Tao et al. 2022; O. A. Johnson et al. 2023). That being said, if a candidate signal observed within the GP passed sky localization filters and had a large scintillation ranking consistent with the expected timescales in that direction, it would be very compelling as a potential technosignature.

Finally, this search was designed to maximize the likelihood of detecting ISM-scintillated technosignatures within relatively short observing times with BL hardware. Though scintillation is a stochastic effect, for the right Δt_d, multiple scintles should be resolved within the course of a single observation. However, we do not know the true values of Δt_d any more than we know what frequency ETI will transmit at, even toward the GC, so we can only estimate using theoretical models for the free electron density and for the distribution of stars in our Galaxy. In the future, we can get higher confidence in our estimates by

updating these models, especially toward the GC (S. K. Ocker & J. M. Cordes 2024).

6. Conclusions

We have presented a *C*-band survey for radio technosignatures toward directions in which ISM scintillation is most detectable, observing 73 targets toward the GC and GP over 24.3 hr. We additionally took a 10 minute scan of the NGP before each observing session, five in total, to analyze the *C*-band RFI environment at the GBT at each observing epoch without risk of observing true ISM-scintillated signals. We developed a procedure for identifying the most probable scintillation timescales as a function of observing parameters, as well as a method for extracting summary statistics relevant to scintillation for every detected narrowband signal. A necessary step of this signal analysis method is to estimate the dedrifted signal bandwidth in time–frequency space, allowing us to report this important property for the first time in a technosignature study.

We do not report any detections of narrowband radio signals that are inconsistent with anthropogenic RFI. Specifically, toward pointings in the GP, we find no evidence of putative radio transmitters with an EIRP above 1.9×10^{17} W up to 8.5 kpc, covering an estimated 6.5 million stars. Likewise, we find no evidence of putative ETI transmitters toward the GC with an EIRP above 7.5×10^{17} W up to 8.5 kpc, covering an estimated 3.5 million stars.

Using synthetic data sets, we developed a ranking procedure to determine the likelihood that a given signal is ISM-scintillated. The method approximates the joint PDF of diagnostic statistics as a function of scintillation timescale and uses a basic maximum likelihood estimation to select the timescale with the highest chance of generating that data. In this work, we limited the specific timescales under consideration to 10, 30, and 100 s. Nevertheless, using a discrete set of candidate timescales suffices for filtering hits and identifying scintillation-like modulation, given our observation parameters.

As a hypothetical, suppose that we had detected a candidate signal that exhibited true ISM scintillations. Then, we would like to fit an accurate scintillation timescale, which would give us some information about where the signal originated along the line of sight through the Galaxy. Knowing the scintillation timescale would also guide efforts for redetection, such as for timing repeat observations and for checking that modulation parameters are consistent. To this end, we could directly expand this paper's method to support any number of candidate timescales, but this would require generating a data set of synthetic signals for every timescale under consideration. This is computationally expensive and does not actually fit a best timescale for the candidate signal. A better approach would be to use approximate Bayesian computation (ABC), which bypasses the estimation of the likelihood function (f_{scint}) by simulating data and comparing to observations (K. Csilléry et al. 2010). We have an end-to-end method for generating synthetic narrowband scintillated signals in noisy radio observations, extracting the intensity time series, and computing summary statistics, so ABC would be well-suited for estimating the most likely scintillation timescales for a given signal.

We find no evidence of scintillated signals toward the GC at the same EIRP limit, but find that the radio frequency environment at the GBT has populations of confounding RFI with scintillation-like intensity modulations. This interestingly depends on the direction in the sky, since observations of the NGP, the direction in which we expect the least to observe true physical scintillation, revealed the highest concentrations of confounding RFI. Getting a better idea of which RFI types are semilocalized on the sky may help future SETI searches and inform which directions are most fruitful for observing potential scintillation. Nevertheless, RFI modulation types vary and are present in high enough quantities that scintillation analysis may not be enough to classify a one-off detection as a legitimate technosignature candidate; we will continue to require that signals both pass sky localization filters and are repeatable for the sake of additional confidence.

Acknowledgments

Breakthrough Listen is managed by the Breakthrough Initiatives, sponsored by the Breakthrough Prize Foundation. The Green Bank Observatory is a facility of the National Science Foundation, operated under cooperative agreement by Associated Universities, Inc. We thank the staff at the Green Bank Observatory for their operational support. B.B. would also like to thank Shelley Wright and Paul Horowitz for helpful discussions. S.Z.S. acknowledges that this material is based upon work supported by the National Science Foundation MPS-Ascend Postdoctoral Research Fellowship under grant No. 2138147.

Software: NumPy (C. R. Harris et al. 2020), SciPy (P. Virtanen et al. 2020), Matplotlib (J. D. Hunter 2007), Jupyter (T. Kluyver et al. 2016), H5py (A. Collette 2013), Pandas (W. McKinney 2010), Astropy (Astropy Collaboration et al. 2013, 2018, 2022), TurboSETI (E. Enriquez & D. Price 2019), Setigen (B. Brzycki et al. 2022; B. Brzycki & R. Donnachie 2024), Blscint (B. Brzycki et al. 2023; B. Brzycki 2024).

Appendix A
Observation Tables

Table 2 details the target list used in this work's survey, including quartiles for expected scintillation timescales estimated from the Monte Carlo–sampling procedure described in Section 2.1. We also include an estimate of the number of stars present within the beam of the GBT at the *C* band up to 8.5 kpc away for each target, which we obtained by numerically integrating the Galactic stellar number density model in Equation (1).

Table 2
Survey Target List

Target	l (deg)	b (deg)	R.A. (J2000)	Decl. (J2000)	Star Count	Δt_d Predictions (s)		
						Q1	Median (Q2)	Q3
GP_L-5_B2	−5.000	2.000	17:25:15.86	−32:03:46.66	8.3×10^4	32.6	52	106
GP_L-4_B2	−4.000	2.000	17:27:52.95	−31:13:59.85	8.6×10^4	32.6	51.3	102
GP_L-3_B2	−3.000	2.000	17:30:27.15	−30:24:00.12	8.9×10^4	32.4	50.7	103
GP_L-2_B2	−2.000	2.000	17:32:58.59	−29:33:48.06	9.1×10^4	32.6	50.6	103
GP_L-1_B2	−1.000	2.000	17:35:27.41	−28:43:24.26	9.3×10^4	32.6	51	104
GP_L0_B2	0.000	2.000	17:37:53.70	−27:52:49.27	9.4×10^4	32.4	50.2	101
GP_L1_B2	1.000	2.000	17:40:17.60	−27:02:03.61	9.3×10^4	32.7	51.1	102
GP_L2_B2	2.000	2.000	17:42:39.20	−26:11:07.80	9.1×10^4	32	50.6	103
GP_L3_B2	3.000	2.000	17:44:58.61	−25:20:02.30	8.9×10^4	33	51.6	106
GP_L4_B2	4.000	2.000	17:47:15.94	−24:28:47.58	8.6×10^4	32.6	51.3	107
GP_L5_B2	5.000	2.000	17:49:31.27	−23:37:24.09	8.3×10^4	32.9	51.5	107
GP_L-5_B1	−5.000	1.000	17:29:11.89	−32:37:09.93	1.2×10^5	15	23.6	48.3
GP_L-4_B1	−4.000	1.000	17:31:47.85	−31:47:03.71	1.2×10^5	15	23.5	48.5
GP_L-3_B1	−3.000	1.000	17:34:20.95	−30:56:45.23	1.2×10^5	14.9	23.1	48.2
GP_L-2_B1	−2.000	1.000	17:36:51.31	−30:06:15.08	1.3×10^5	15.1	23.6	49
GP_L-1_B1	−1.000	1.000	17:39:19.05	−29:15:33.83	1.3×10^5	0.201	8.49	29.1
GP_L0_B1	0.000	1.000	17:41:44.30	−28:24:42.01	1.3×10^5	4.73	13.8	31.6
GP_L1_B1	1.000	1.000	17:44:07.16	−27:33:40.14	1.3×10^5	15.2	23.6	47.7
GP_L2_B1	2.000	1.000	17:46:27.76	−26:42:28.71	1.3×10^5	15	23.7	47
GP_L3_B1	3.000	1.000	17:48:46.19	−25:51:08.18	1.2×10^5	15.3	23.9	47.6
GP_L4_B1	4.000	1.000	17:51:02.56	−24:59:39.01	1.2×10^5	15.3	24	49.1
GP_L5_B1	5.000	1.000	17:53:16.97	−24:08:01.62	1.2×10^5	16.3	25.7	55.2
GP_L-5_B0	−5.000	0.000	17:33:10.84	−33:10:05.27	1.6×10^5	10.3	16.5	33.4
GP_L-4_B0	−4.000	0.000	17:35:45.56	−32:19:40.30	1.7×10^5	10.5	16.3	31.9
GP_L-3_B0	−3.000	0.000	17:38:17.42	−31:29:03.75	1.7×10^5	10.4	15.8	31.5
GP_L-2_B0	−2.000	0.000	17:40:46.56	−30:38:16.19	1.8×10^5	10.3	16.1	32.2
GP_L-1_B0	−1.000	0.000	17:43:13.12	−29:47:18.18	1.8×10^5	10.4	16.4	32.5
GP_L1_B0	1.000	0.000	17:47:58.92	−28:04:52.87	1.8×10^5	10.5	16	31.9
GP_L2_B0	2.000	0.000	17:50:18.41	−27:13:26.54	1.8×10^5	10.4	16.1	31.8
GP_L3_B0	3.000	0.000	17:52:35.76	−26:21:51.70	1.7×10^5	10.3	16.2	32.7
GP_L4_B0	4.000	0.000	17:54:51.08	−25:30:08.81	1.7×10^5	10.4	16.1	32.2
GP_L5_B0	5.000	0.000	17:57:04.47	−24:38:18.26	1.6×10^5	11.5	18.1	37.6
GP_L-5_B-1	−5.000	−1.000	17:37:12.79	−33:42:31.73	1.2×10^5	15.1	24.1	51
GP_L-4_B-1	−4.000	−1.000	17:39:46.11	−32:51:48.70	1.2×10^5	15.2	24	48.8
GP_L-3_B-1	−3.000	−1.000	17:42:16.61	−32:00:54.79	1.3×10^5	15.1	23.8	49.3
GP_L-2_B-1	−2.000	−1.000	17:44:44.41	−31:09:50.54	1.3×10^5	15.1	23.7	47
GP_L-1_B-1	−1.000	−1.000	17:47:09.65	−30:18:36.49	1.3×10^5	15.2	23.8	48.5
GP_L0_B-1	0.000	−1.000	17:49:32.45	−29:27:13.16	1.3×10^5	15.1	24.3	49.7
GP_L1_B-1	1.000	−1.000	17:51:52.93	−28:35:41.02	1.3×10^5	15.1	23.5	48.8
GP_L2_B-1	2.000	−1.000	17:54:11.19	−27:44:00.54	1.3×10^5	15.1	23.6	48.1
GP_L3_B-1	3.000	−1.000	17:56:27.36	−26:52:12.15	1.3×10^5	15.1	23.7	47.7
GP_L4_B-1	4.000	−1.000	17:58:41.53	−26:00:16.28	1.2×10^5	15.1	23.6	47.4
GP_L5_B-1	5.000	−1.000	18:00:53.81	−25:08:13.32	1.2×10^5	16.3	26	57.4
GP_L-5_B-2	−5.000	−2.000	17:41:17.77	−34:14:28.34	8.5×10^4	33.3	52.9	109
GP_L-4_B-2	−4.000	−2.000	17:43:49.57	−33:23:27.99	8.8×10^4	0.122	28	70.1
GP_L-3_B-2	−3.000	−2.000	17:46:18.56	−32:32:17.44	9.0×10^4	32.6	50.7	106
GP_L-2_B-2	−2.000	−2.000	17:48:44.90	−31:40:57.25	9.3×10^4	32.3	50.5	105
GP_L-1_B-2	−1.000	−2.000	17:51:08.70	−30:49:27.93	9.4×10^4	32.3	50.8	104
GP_L0_B-2	0.000	−2.000	17:53:30.10	−29:57:49.97	9.5×10^4	32.6	50.8	102
GP_L1_B-2	1.000	−2.000	17:55:49.21	−29:06:03.83	9.4×10^4	32.7	51.8	105
GP_L2_B-2	2.000	−2.000	17:58:06.15	−28:14:09.96	9.3×10^4	32.4	50.3	104
GP_L3_B-2	3.000	−2.000	18:00:21.03	−27:22:08.79	9.0×10^4	33.1	51.7	109
GP_L4_B-2	4.000	−2.000	18:02:33.95	−26:30:00.73	8.8×10^4	33.2	52.1	107
GP_L5_B-2	5.000	−2.000	18:04:45.01	−25:37:46.15	8.5×10^4	33.2	52	107
GC_A00	−0.056	−0.046	17:45:40.04	−29:00:28.10	1.8×10^5	0.00693	0.144	18.5
GC_C01	0.028	−0.046	17:45:51.95	−28:56:11.99	1.8×10^5	0.00692	0.0604	18.5
GC_C07	−0.139	−0.046	17:45:28.12	−29:04:44.14	1.8×10^5	0.00696	0.0716	18.8
GC_B01	−0.014	−0.046	17:45:45.99	−28:58:20.05	1.8×10^5	0.00699	0.0836	18.7
GC_B04	−0.097	−0.046	17:45:34.08	−29:02:36.13	1.8×10^5	0.00687	0.0649	18.3
GC_B02	−0.035	−0.010	17:45:34.57	−28:58:16.40	1.8×10^5	0.00738	0.0601	19
GC_B05	−0.077	−0.082	17:45:45.52	−29:02:39.78	1.8×10^5	0.00625	0.0519	18.2
GC_B03	−0.077	−0.010	17:45:28.61	−29:00:24.42	1.8×10^5	0.00781	0.117	18.9
GC_B06	−0.035	−0.082	17:45:51.47	−29:00:31.72	1.8×10^5	0.00652	0.0952	19.2

Table 2
(Continued)

Target	l (deg)	b (deg)	R.A. (J2000)	Decl. (J2000)	Star Count	Δt_d Predictions (s)		
						Q1	Median (Q2)	Q3
GC_C02	0.007	−0.010	17:45:40.52	−28:56:08.37	1.8×10^5	0.00749	0.0587	18.5
GC_C04	−0.056	0.026	17:45:23.14	−28:58:12.69	1.8×10^5	0.0104	0.106	19.4
GC_C03	−0.014	0.026	17:45:29.10	−28:56:04.69	1.8×10^5	0.0101	0.0921	19.1
GC_C05	−0.097	0.026	17:45:17.18	−29:00:20.67	1.8×10^5	0.0102	0.0925	18.6
GC_C08	−0.118	−0.082	17:45:39.56	−29:04:47.83	1.8×10^5	0.00652	0.0763	19.2
GC_C06	−0.118	−0.010	17:45:22.65	−29:02:32.42	1.8×10^5	0.00768	0.0849	18.7
GC_C11	−0.014	−0.118	17:46:02.90	−29:00:35.29	1.8×10^5	0.00652	0.142	18.7
GC_C09	−0.097	−0.118	17:45:51.00	−29:04:51.46	1.8×10^5	0.00664	0.101	19.2
GC_C10	−0.056	−0.118	17:45:56.95	−29:02:43.38	1.8×10^5	0.00638	0.0988	19.1
GC_C12	0.007	−0.082	17:45:57.42	−28:58:23.65	1.8×10^5	0.00681	0.0929	18.9

Appendix B
NGP Statistics

Figure 18 compares the distribution of drift rates and S/Ns of hit signals detected in each of the five NGP observations. We readily observe that NGP3 has the most unique spread in detected drift rates, whereas the S/N distributions seem relatively similar.

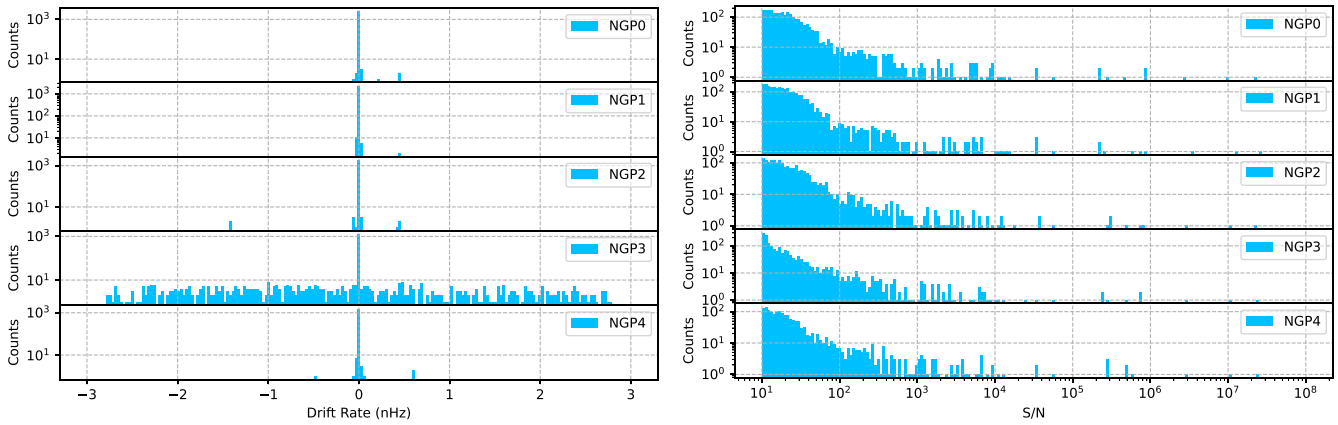

(a) Distribution of hit drift rates

(b) Distribution of hit S/N ratios

Figure 18. Histograms of drift rates and S/Ns of detected hits in each NGP observation.

Appendix C
Candidate Vetting

Figure 19 displays the full cadence comparison performed for the two best candidate events found in this work, as described in Section 4.2. In both cases, we find evidence of the same signal morphology recurring close in frequency throughout each observing session, implying that the signal sources are not localized in the sky.

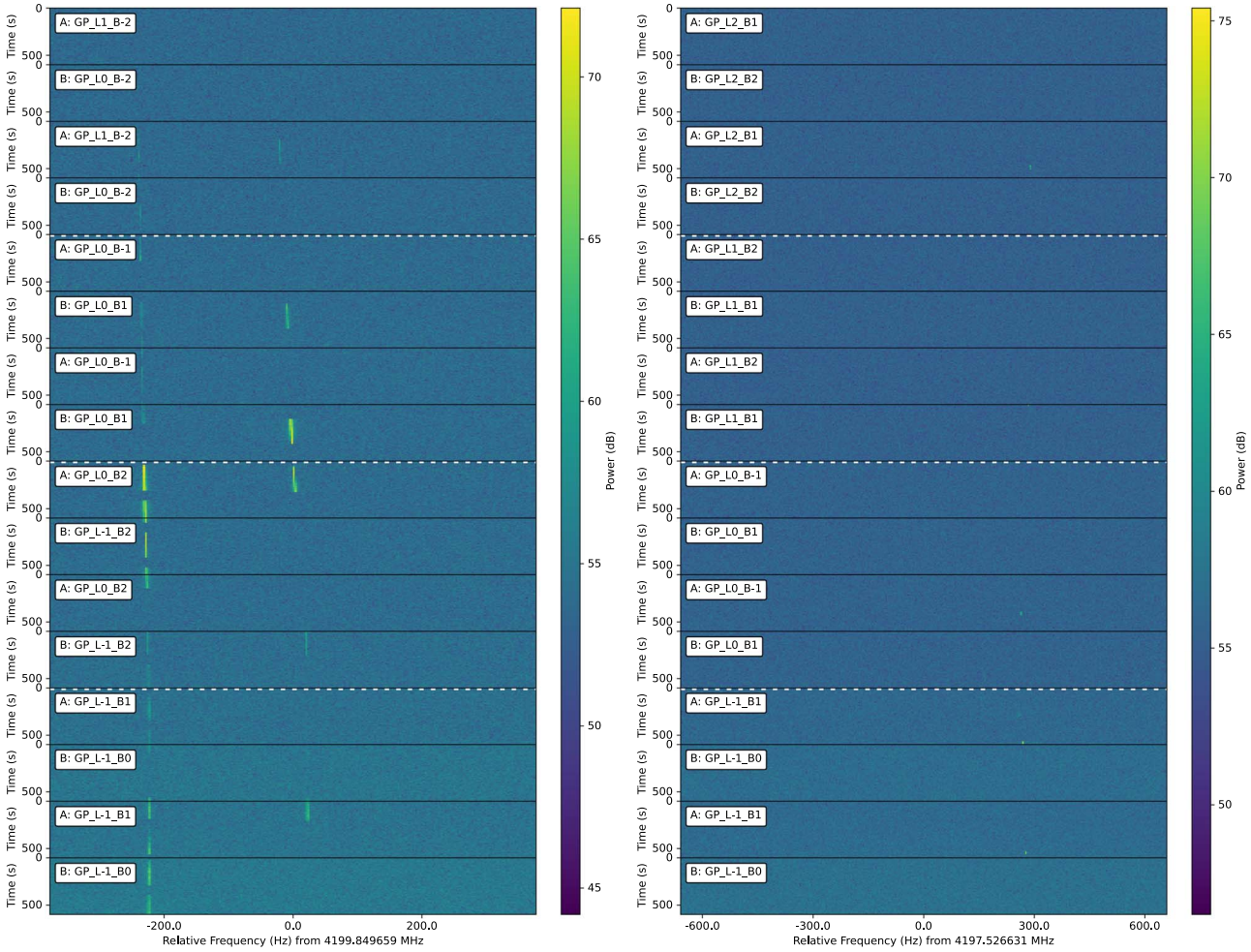

(a) (b)

Figure 19. Extended plots of adjacent cadences for the highest-quality candidates that passed the directional filter.

ORCID iDs

Bryan Brzycki https://orcid.org/0000-0002-7461-107X
Andrew P. V. Siemion https://orcid.org/0000-0003-2828-7720
Imke de Pater https://orcid.org/0000-0002-4278-3168
Carmen Choza https://orcid.org/0009-0008-0662-1293
Steve Croft https://orcid.org/0000-0003-4823-129X
Vishal Gajjar https://orcid.org/0000-0002-8604-106X
Brian C. Lacki https://orcid.org/0000-0003-1515-4857
Danny C. Price https://orcid.org/0000-0003-2783-1608
Sofia Z. Sheikh https://orcid.org/0000-0001-7057-4999

References

Acharyya, A., Adams, C. B., Archer, A., et al. 2023, AJ, 166, 84
Astropy Collaboration, Price-Whelan, A. M., Lim, P. L., et al. 2022, ApJ, 935, 167
Astropy Collaboration, Price-Whelan, A. M., Sipőcz, B. M., et al. 2018, AJ, 156, 123
Astropy Collaboration, Robitaille, T. P., Tollerud, E. J., et al. 2013, A&A, 558, A33
Backus, P. R., Laroque, S., Tarter, J. C., et al. 1997, in IAU Colloq. 161: Astronomical and Biochemical Origins and the Search for Life in the Universe, ed. C. Batalli Cosmovici, S. Bowyer, & D. Werthimer (Cambridge: Cambridge Univ. Press), 661
Backus, P. & Project Phoenix Team 2002, in ASP Conf. Ser. 278, Single-Dish Radio Astronomy: Techniques and Applications, ed. S. Stanimirovic et al. (San Francisco, CA: ASP), 525
Brzycki, B. 2024, bbrzycki/blscint: v1.0.0, Zenodo, doi:10.5281/zenodo.13820386
Brzycki, B., & Donnachie, R. 2024, bbrzycki/setigen: v2.7.0, Zenodo, doi:10.5281/zenodo.13178628
Brzycki, B., Siemion, A. P., de Pater, I., et al. 2022, AJ, 163, 222
Brzycki, B., Siemion, A. P. V., de Pater, I., et al. 2023, ApJ, 952, 46
Carroll, B., & Ostlie, D. 2007, An Introduction to Modern Astrophysics (Reading, MA: Addison-Wesley)
Choza, C., Bautista, D., Croft, S., et al. 2023, AJ, 167, 10
Collette, A. 2013, in Python and HDF5: Unlocking Scientific Data, ed. M. Blanchette & R. Roumeliotis (Sebastopol, CA: O'Reilly Media)
Cordes, J. M., & Lazio, T. J. 1991, ApJ, 376, 123
Cordes, J. M., & Lazio, T. J. W. 2002, arXiv:astro-ph/0207156
Csilléry, K., Blum, M. G., Gaggiotti, O. E., & François, O. 2010, TEcoE, 25, 410
Drake, F., Wolfe, J. H., & Seeger, C. L. 1984, SETI Science Working Group Report NASA-TP-2244, NASA
Enriquez, E., & Price, D. 2019, turboSETI: Python-based SETI Search Algorithm, Astrophysics Source Code Library, ascl:1906.006
Enriquez, J. E., Siemion, A., Foster, G., et al. 2017, ApJ, 849, 104
Gajjar, V., LeDuc, D., Chen, J., et al. 2022, ApJ, 932, 81
Gajjar, V., Perez, K. I., Siemion, A. P. V., et al. 2021, AJ, 162, 33
Garrett, M. A., & Siemion, A. P. V. 2023, MNRAS, 519, 4581
GBT Support Staff 2017, The Proposer's Guide for the Green Bank Telescope, Green Bank Observatory, https://www.gb.nrao.edu/scienceDocs/GBTpg.pdf
Gowanlock, M. G., Patton, D. R., & McConnell, S. M. 2011, AsBio, 11, 855
Gray, R. H. 2020, AJ, 159, 228
Gray, R. H., & Mooley, K. 2017, AJ, 153, 110
Harp, G. R., Richards, J., Tarter, J. C., et al. 2016, AJ, 152, 181
Harris, C. R., Millman, K. J., van der Walt, S. J., et al. 2020, Natur, 585, 357
Hickish, J., Abdurashidova, Z., Ali, Z., et al. 2016, JAI, 5, 1641001
Horowitz, P., & Sagan, C. 1993, ApJ, 415, 218
Hunter, J. D. 2007, CSE, 9, 90
Isaacson, H., Siemion, A. P. V., Marcy, G. W., et al. 2017, PASP, 129, 054501
Johnson, O. A., Gajjar, V., Keane, E. F., et al. 2023, AJ, 166, 193
Kardashev, N. S. 1964, SvA, 8, 217
Kluyver, T., Ragan-Kelley, B., Pérez, F., et al. 2016, in Positioning and Power in Academic Publishing: Players, Agents and Agendas, ed. F. Loizides & B. Schmidt (Amsterdam: IOS Press), 87
Lebofsky, M., Croft, S., Siemion, A. P. V., et al. 2019, PASP, 131, 124505
Li, M. G., Sheikh, S. Z., Gilbertson, C., et al. 2023, AJ, 166, 182
Lipman, D., Isaacson, H., Siemion, A. P. V., et al. 2019, PASP, 131, 034202
Maan, Y., van Leeuwen, J., & Vohl, D. 2021, A&A, 650, A80
MacMahon, D. H. E., Price, D. C., Lebofsky, M., et al. 2018, PASP, 130, 044502
Margot, J.-L., Li, M. G., Pinchuk, P., et al. 2023, AJ, 166, 206
Margot, J.-L., Pinchuk, P., Geil, R., et al. 2021, AJ, 161, 55
McKinney, W. 2010, Proc. 9th Python in Science Conf., ed. W. Stéfan van der & M. Jarrod (Austin, TX: SciPy), 51
Morrison, I. S., & Gowanlock, M. G. 2015, AsBio, 15, 683
Nilipour, A., Davenport, J. R. A., Croft, S., & Siemion, A. P. V. 2023, AJ, 166, 79
Ocker, S. K., & Cordes, J. M. 2024, RNAAS, 8, 17
Parsons, A., Backer, D., Chang, C., et al. 2006, in 2006 Fortieth Asilomar Conf. on Signals, Systems and Computers, ed. M. B. Matthews (Piscataway, NJ: IEEE), 2031
Price, D. C., Enriquez, J. E., Brzycki, B., et al. 2020, AJ, 159, 86
Price, D. C., MacMahon, D. H. E., Lebofsky, M., et al. 2018, PASA, 35, 41
Radovan, M. V., Lanclos, K., Holden, B. P., et al. 2014, Proc. SPIE, 9145, 91452B
Rajwade, K. M., Lorimer, D. R., & Anderson, L. D. 2017, MNRAS, 471, 730
Rogers, B., Lintott, C. J., Croft, S., Schwamb, M. E., & Davenport, J. R. A. 2024, AJ, 167, 118
Scott, D. W. 2015, Multivariate Density Estimation: Theory, Practice, and Visualization (New York: Wiley)
Sheikh, S. Z., Smith, S., Price, D. C., et al. 2021, NatAs, 5, 1153
Sheikh, S. Z., Wright, J. T., Siemion, A., & Enriquez, J. E. 2019, ApJ, 884, 14
Siemion, A. P. V., Demorest, P., Korpela, E., et al. 2013, ApJ, 767, 94
Stone, R. P. S., Wright, S. A., Drake, F., et al. 2005, AsBio, 5, 604
Suresh, A., Cordes, J. M., Chatterjee, S., et al. 2021, ApJ, 921, 101
Suresh, A., Gajjar, V., Nagarajan, P., et al. 2023, AJ, 165, 255
Tao, Z.-Z., Zhao, H.-C., Zhang, T.-J., et al. 2022, AJ, 164, 160
Tarter, J. 2001, ARA&A, 39, 511
Taylor, J. H. 1974, A&AS, 15, 367
Tremblay, C. D., & Tingay, S. J. 2020, PASA, 37, e035
Uno, Y., Hashimoto, T., Goto, T., et al. 2023, MNRAS, 522, 4649
Virtanen, P., Gommers, R., Oliphant, T. E., et al. 2020, NatMe, 17, 261
Worden, S. P., Drew, J., Siemion, A., et al. 2017, AcAau, 139, 98
Wright, J. T., Kanodia, S., & Lubar, E. 2018a, AJ, 156, 260
Wright, S. A., Horowitz, P., Maire, J., et al. 2018b, Proc. SPIE, 10702, 107025I
Yao, J. M., Manchester, R. N., & Wang, N. 2017, ApJ, 835, 29
Zuckerman, A., Davenport, J. R. A., Croft, S., Siemion, A., & de Pater, I. 2024, AJ, 167, 20
Zuckerman, A., Ko, Z., Isaacson, H., et al. 2023, AJ, 165, 114